

General High-Frequency-Link Analysis and Application of Dual Active Bridge Converters

Ziheng Xiao , Zhixing He , Member, IEEE, Hongliang Wang , Senior Member, IEEE, An Luo, Senior Member, IEEE, Zhikang Shuai , Senior Member, IEEE, and Josep M. Guerrero , Fellow, IEEE

Abstract—High-frequency-link (HFL) electrical quantities, including high-frequency voltages, currents, and instantaneous power, are closely related to the performance of dc–dc converters. However, HFL electrical quantities are usually square, triangular, or trapezoidal waves and conventional indicators like apparent power or power factor are with vague physical meaning. This article gives a general HFL analysis to guide the optimization of dual active bridge converters (DAB). Novel indicators are proposed to describe the instantaneous power characteristic, which show better accuracy and reliability than the conventional indicators. Optimization objective construction method and hybrid optimization algorithm are proposed to calculate the optimal control coordinate, and the efficiency of DAB is enhanced for most of the operation points. Besides, the novel indicators and optimization objective are also good at the estimation of efficiency. Finally, experimental results verified the validity of the HFL analysis.

Index Terms—Dual active bridge converters (DAB), high-frequency link (HFL), instantaneous power, modulation schemes.

I. INTRODUCTION

QUESTIONS like how to define reactive power and how to understand different terms of apparent power have been discussed for a very long time, especially under nonsinusoidal voltage and current conditions [1]–[6]. In 1927, Budeanu realized there were more than two components of the apparent power of a nonsinusoidal system and could be displayed in a three-dimensional map, which is the well-known Budeanu theory [2]. In 1931, Fryze decomposed the current into an active current with the same waveform and phase with voltage and the remaining part is defined as reactive current [3]–[5]. The p – q theory was proposed and continuously improved by Akagi and Nabae in 1983 [6]. Paolo Tenti and Paolo Mattavelli proposed the conservative power theory (CPT) in [7] and a framework for smart microgrid description and control problems based on CPT

was proposed in [8]. From the Budeanu and Fryze power theory to the subsequent p – q theory, and CPT, they played a significant role in the definition and compensation of reactive power in the ac power system [6]–[9].

With the development of power electronics, dc–dc converters like phase-shift full bridge converters (PSFB), resonant or multiresonant converters, and dual active bridge converters (DAB) are widely adopted in battery charger [10]–[12], automotive application [13]–[16], solid-state transformer [17]–[22], photovoltaic application [23], [24], and dc microgrid [25], [26]. With the advantage of bidirectional buck and boost power transmission capability, intrinsic soft-switching characteristics and high power density, DAB attracts more and more attention both in the academic and industrial circles. The high-frequency link (HFL) electrical quantities of DAB [27], including high-frequency voltage, current, and instantaneous power, whose main waveforms are square, triangle, or trapezoidal waves, are the category of nonsinusoidal conditions. As for the HFL current analysis of DAB, [28]–[31] focused on reducing peak current I_{Peak} and [32]–[34] gave a comprehensive analysis of DAB with minimum I_{rms} . The switches are with the lowest current stress when minimum I_{Peak} is achieved and the conduction and copper losses is minimized when minimum I_{rms} is adopted. As for the HFL power analysis of DAB, [35] gave the power flow characteristic of DAB, [36] discussed circulating power of DAB with single-phase-shift (SPS) modulation scheme. [37]–[39] discussed the power characterization of DAB with dual-phase-shift (DPS) modulation scheme. Zhao *et al.* [10] pointed out a phenomenon of power backflow in SPS and proposed extended-phase-shift (EPS) modulation scheme to reduce power backflow. When the power backflow is reduced to zero, the special case in EPS is termed as zero circulating power modulation scheme (ZCPM) in this article [10]. The minimization of reactive or nonactive power was reported in [40]–[42]. A practical HFL fundamental-optimal modulation scheme (FOM) was proposed in [27] to maximize fundamental power transmission. Wang *et al.* [43] discussed the reactive components and power factor of DAB with triple-phase-shift (TPS) control. Fourier decomposition was applied to phase shift, duty ratios, and indicator current in the generalized average model for DAB in [44]–[46]. Essentially, the generalized average model for DAB is dealing with infinity series and its derivatives. However, the analysis of instantaneous power is more complex because it is dealing with the multiplication of two infinity series.

The above literature provided some explanations for the nonsinusoidal current and nonactive power in the HFL of DAB.

Manuscript received August 12, 2019; revised November 5, 2019; accepted December 25, 2019. Date of publication January 5, 2020; date of current version April 22, 2020. This work was supported in part by the National Natural Science Foundation of China under Grant 51807057, and in part by the Hunan Natural Science Foundation Funded Project under Grant 2019JJ50038. Recommended for publication by Associate Editor J. Biela. (Corresponding author: Zhixing He.)

Z. Xiao, Z. He, H. Wang, A. Luo, and Z. Shuai are with the College of Electrical and Information Engineering, Hunan University, Changsha 410082, China (e-mail: zihengxiao@hnu.edu.cn; hezhixingmail@163.com; liangliang-930@163.com; an_luo@126.com; szk@hnu.edu.cn).

J. M. Guerrero is with the Department of Energy Technology, Aalborg University, Aalborg East 9220, Denmark (e-mail: joz@et.aau.dk).

Color versions of one or more of the figures in this article are available online at <http://ieeexplore.ieee.org>.

Digital Object Identifier 10.1109/TPEL.2019.2963746

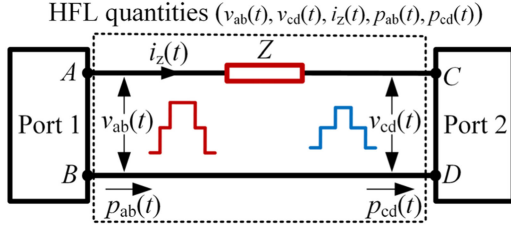


Fig. 1. Two one-port network model.

The currents with no effective power transmission are usually termed as circulating current, backflow current, reactive current, or freewheeling current. Although they pointed out that these currents would increase I_{rms} , an accurate mathematical description of this essence is insufficient.

In order to provide a clear mathematical description of non-sinusoidal current and nonactive power in the HFL of DAB, this article gave a general HFL analysis based on the orthogonal decomposition of voltage, current, and instantaneous power. Instantaneous power is decomposed into dc power (average power) and fluctuation power. Novel indicators are proposed to describe the dc power component percentage from the perspective of signal strength and energy. With the proposed novel indicators, the instantaneous power characteristic is better described. Optimization objective construction method and hybrid optimization algorithm are proposed to calculate the optimal control coordinate with higher indicators. The optimal control coordinate shows higher efficiency compared with other schemes in most of the operation points. Besides, the novel indicators and optimization objective are also good at the estimation of efficiency for an arbitrary voltage gain and power transmission condition.

This article is further organized as follows. In Section II, the basic decomposition of the HFL voltage and current are derived. On this basis, instantaneous power and apparent power are deduced and novel indicators are proposed. Multiple modulation schemes of DAB are analyzed in Section III-A comparison of the modulation schemes mentioned above is made in Section IV, and a multiindicator evaluation and optimization for DAB is established to enhance the efficiency of DAB. The experimental results are included in Section V. Finally, the conclusion is drawn in Section VI, and it is followed by a discussion on the application of multiple dc-dc converters presented in Section VII.

II. GENERAL HFL ANALYSIS

The model of two one-port networks interconnected with impedance Z is adopted to illustrate the general HFL analysis, which is depicted in Fig. 1, where the HFL quantities are instantaneous voltage $v_{ab}(t)$, $v_{cd}(t)$, instantaneous current $i_z(t)$, and instantaneous power $p_{ab}(t)$, $p_{cd}(t)$.

Based on the generalized averaging concept in [47], any periodic waveform satisfying Dirichlet conditions can be approximated to an arbitrary degree by its discrete Fourier series

as follows:

$$\begin{aligned} x(t) &\approx \sum_{h=-n}^n X_h e^{jh\omega t} \\ &= \sqrt{2} \sum_{h=-n}^n (a_{ch} \cos(h\omega t) + a_{sh} \sin(h\omega t)) \end{aligned} \quad (1)$$

where X_h , ω , h , and n are Fourier series coefficient, fundamental frequency, the order, and the total number of harmonics, respectively.

$v_{ab}(t)$, $v_{cd}(t)$, and $i_z(t)$ can be decomposed to Fourier series as

$$\begin{cases} v_{ab}(t) = v_{abc}(t) + v_{abs}(t) \\ \quad \approx \sqrt{2} \sum_{h=-n}^n (a_{ch} \cos(h\omega t) + a_{sh} \sin(h\omega t)) \\ v_{cd}(t) = v_{cdc}(t) + v_{c ds}(t) \\ \quad \approx \sqrt{2} \sum_{h=-n}^n (b_{ch} \cos(h\omega t) + b_{sh} \sin(h\omega t)) \\ i_z(t) = i_{zc}(t) + i_{zs}(t) \\ \quad \approx \sqrt{2} \sum_{h=-n}^n (c_{ch} \cos(h\omega t) + c_{sh} \sin(h\omega t)) \end{cases} \quad (2)$$

where $v_{abc}(t)$, $v_{abs}(t)$, $v_{cdc}(t)$, $v_{c ds}(t)$, $i_{zc}(t)$, and $i_{zs}(t)$ are cosine and sine terms of $v_{ab}(t)$, $v_{cd}(t)$, and $i_z(t)$, respectively, and a_{ch} , a_{sh} , b_{ch} , b_{sh} , c_{ch} , and c_{sh} are the h th order Fourier series coefficient of sine terms and cosine terms of $v_{ab}(t)$, $v_{cd}(t)$, and $i_z(t)$, respectively.

$p_{ab}(t)$ and $p_{cd}(t)$ are given as

$$\begin{aligned} p_{ab}(t) &= v_{ab}(t) \cdot i_z(t) = (v_{abc}(t) + v_{abs}(t)) \cdot (i_{zc}(t) \\ &\quad + i_{zs}(t)) \\ p_{cd}(t) &= v_{cd}(t) \cdot i_z(t) = (v_{cdc}(t) + v_{c ds}(t)) \cdot (i_{zc}(t) \\ &\quad + i_{zs}(t)). \end{aligned} \quad (3)$$

The above coefficients form six vectors \mathbf{v}_{abc} , \mathbf{v}_{abs} , \mathbf{v}_{cdc} , $\mathbf{v}_{c ds}$, \mathbf{i}_{zc} , and \mathbf{i}_{zs} to describe $v_{ab}(t)$, $v_{cd}(t)$, and $i_z(t)$, where

$$\begin{aligned} \mathbf{v}_{abc} &= [a_{c1}, a_{c2}, \dots, a_{cn}]^T, \mathbf{v}_{abs} = [a_{s1}, a_{s2}, \dots, a_{sn}]^T \\ \mathbf{v}_{cdc} &= [b_{c1}, b_{c2}, \dots, b_{cn}]^T, \mathbf{v}_{c ds} = [b_{s1}, b_{s2}, \dots, b_{sn}]^T \\ \mathbf{i}_{zc} &= [c_{c1}, c_{c2}, \dots, c_{cn}]^T, \mathbf{i}_{zs} = [c_{s1}, c_{s2}, \dots, c_{sn}]^T. \end{aligned} \quad (4)$$

A. Instantaneous Power Analysis

According to (3) and (4), four matrices \mathbf{S}_{abcc} , \mathbf{S}_{abcs} , \mathbf{S}_{absc} , and \mathbf{S}_{abss} are derived to describe $p_{ab}(t)$ as $\mathbf{S}_{abcc} = \mathbf{v}_{abc}^T \mathbf{i}_{zc}$, $\mathbf{S}_{abcs} = \mathbf{v}_{abc}^T \mathbf{i}_{zs}$, $\mathbf{S}_{absc} = \mathbf{v}_{abs}^T \mathbf{i}_{zc}$, and $\mathbf{S}_{abss} = \mathbf{v}_{abs}^T \mathbf{i}_{zs}$. The expressions of \mathbf{S}_{abcc} , \mathbf{S}_{abcs} , \mathbf{S}_{absc} , and \mathbf{S}_{abss} are given in the Appendix. As for $p_{cd}(t)$, similar matrices \mathbf{S}_{cdcc} , \mathbf{S}_{cdcs} , \mathbf{S}_{cdsc} , and \mathbf{S}_{cdss} can be obtained and the analysis is similar. Hence, the following instantaneous power analysis only focuses on $p_{ab}(t)$.

The multiplication of two trigonometric functions can be decomposed to the frequency sum term and frequency difference term. As for voltage and current with identical frequency $i\omega$, two sine terms or two cosine terms generate the dc power

component p_{ab0ic} and second-order harmonic power component p_{ab2ic} , while sine and cosine term only generate second-order harmonic power component p_{ab2is} .

Since dc power can only be generated by voltage and current with identical frequency and identical trigonometric functions, the total dc power p_{ab0c} is given as

$$p_{ab0c} = \sum_{j=1}^n (a_{cj}c_{cj} + a_{sj}c_{sj}). \quad (5)$$

p_{ab0c} can also be expressed as $p_{ab0c} = \text{Tr}(\mathbf{S}_{abcc}) + \text{Tr}(\mathbf{S}_{abss})$, where $\text{Tr}(\mathbf{A})$ is the trace of matrix \mathbf{A} . Exclude p_{ab0c} from $p_{ab}(t)$, and the remaining part is defined as fluctuation power p_{abf} [fluctuation power of $p_{cd}(t)$ is denoted as p_{cdf}]. Because the integration of p_{abf} in one fundamental cycle $1/\omega$ is zero, p_{abf} does not contribute to effective power transmission. p_{abf} is always accompanied by dc power, and it will cause higher I_{rms} and undesired losses. Hence, p_{abf} should be as small as possible.

p_{ab0ic} has a byproduct second-order harmonic power p_{ab2ic} , and the total second-order harmonic power is denoted as P_{ab2c} , where

$$P_{ab2c} = \sum_{i=1}^n p_{ab2ic} = \sum_{j=1}^n (a_{cj}c_{cj} - a_{sj}c_{sj}) \cos(2j\omega t). \quad (6)$$

p_{ab2is} is with the same concept of reactive power in Budeanu power theory generated by voltage and current with identical frequency but orthogonal. Hence, the total reactive power is denoted as P_{ab2s} where

$$P_{ab2s} = \sum_{i=1}^n p_{ab2is} = \sum_{j=1}^n (a_{cj}c_{sj} + a_{sj}c_{cj}) \sin(2j\omega t). \quad (7)$$

p_{ab0c} , P_{ab2c} , and P_{ab2s} are only related to the main diagonal of \mathbf{S}_{abcc} , \mathbf{S}_{abcs} , \mathbf{S}_{absc} , and \mathbf{S}_{abss} . Exclude P_{ab2c} and P_{ab2s} from p_{abf} , and the remaining parts are generated by voltage and current with different frequencies only related to the nonmain diagonal of \mathbf{S}_{abcc} , \mathbf{S}_{abcs} , \mathbf{S}_{absc} , and \mathbf{S}_{abss} .

After getting the discrete Fourier series of $v_{ab}(t)$ and $i_z(t)$, the discrete Fourier series of $p_{ab}(t)$ can be derived. The coefficient of every term in $p_{ab}(t)$ is related to discrete convolution and discrete correlation of $v_{ab}(t)$ and $i_z(t)$. The coefficients of sine and cosine terms of $p_{ab}(t)$ with frequency $r\omega$ are denoted as p_{abrs} and p_{abrc} , where

$$\begin{aligned} p_{abrc} &= r_{cc}(r) + r_{ss}(r) + s_{cc}(r) - s_{ss}(r) \\ p_{abrs} &= r_{sc}(r) - r_{cs}(r) + s_{sc}(r) - s_{cs}(r). \end{aligned} \quad (8)$$

$s_{xy}(r)$ and $r_{xy}(r)$ are discrete convolution and discrete correlation with frequency $r\omega$ and are given as

$$s_{xy}(r) = \sum_{i=1}^n a_{xi}c_{y(r-i)}, r_{xy}(r) = \sum_{i=1}^n a_{x(r+i)}c_{yi} \quad (9)$$

where the subscript x and y represent sine term (denoted as s) and cosine term (denoted as c), respectively.

Noted that the discrete Fourier series of $p_{ab}(t)$ generated by (8) and (9) is different from the discrete Fourier series of $p_{ab}(t)$ due

to the truncation error. However, the truncation error decreases rapidly with the increasing of n .

On combining (5) to (9), $p_{ab}(t)$ is approximately given as

$$p_{ab}(t) \approx p_{ab0c} + \sum_{r=1}^{2n} p_{abrs} \sin(r\omega t) + \sum_{r=1}^{2n} p_{abrc} \cos(r\omega t). \quad (10)$$

Since every component in $p_{ab}(t)$ is orthogonal to the rest of the other components, (10) is an orthogonal decomposition of $p_{ab}(t)$. Hence, $p_{ab}(t)$ can be expressed as space vector formula with $p_{ab}(t) = [p_{ab0c} p_{ab1s} p_{ab2s} \cdots p_{ab2ns} p_{ab1c} p_{ab2c} \cdots p_{ab2nc}]$. In order to compare different $p_{ab}(t)$ s when p_{ab0c} are identical, the space vector analysis of signal is introduced.

The strength of $p_{ab}(t)$ is given as the one-norm of $p_{ab}(t)$, where

$$\|p_{ab}(t)\|_1 = |p_{ab0c}| + \sum_{r=1}^{2n} (|p_{abrs}| + |p_{abrc}|). \quad (11)$$

The energy of $p_{ab}(t)$ is given as the square of the two-norm of $p_{ab}(t)$, and the two-norm of $p_{ab}(t)$ is given as

$$\|p_{ab}(t)\|_2 = \sqrt{(p_{ab0c})^2 + \sum_{r=1}^{2n} ((p_{abrs})^2 + (p_{abrc})^2)}. \quad (12)$$

B. Apparent Power Analysis

The rms values of $v_{ab}(t)$ and $i_z(t)$ are denoted as v_{abrms} and i_{zrms} , and the apparent power S_{ab} is given as

$$\begin{aligned} S_{ab} &= v_{abrms} \cdot i_{zrms} \\ &= \sqrt{\left(\sum_{i=1}^n (a_{ci}^2 + a_{si}^2)\right) \left(\sum_{i=1}^n (c_{ci}^2 + c_{si}^2)\right)} \\ &= \sqrt{\sum_{i=1}^n a_{ci}^2 \sum_{i=1}^n c_{ci}^2 + \sum_{i=1}^n a_{ci}^2 \sum_{i=1}^n c_{si}^2} \\ &\quad + \sum_{i=1}^n a_{si}^2 \sum_{i=1}^n c_{ci}^2 + \sum_{i=1}^n a_{si}^2 \sum_{i=1}^n c_{si}^2. \end{aligned} \quad (13)$$

According to Lagrange identity, there is

$$\left\{ \begin{aligned} \sum_{i=1}^n a_{ci}^2 \sum_{i=1}^n c_{ci}^2 &= \sum_{i=1}^n a_{ci}^2 c_{ci}^2 \\ &\quad + \sum_{i=1}^{n-1} \sum_{j=i+1}^n (a_{ci}c_{cj} - a_{cj}c_{ci})^2 \\ \sum_{i=1}^n a_{ci}^2 \sum_{i=1}^n c_{si}^2 &= \sum_{i=1}^n a_{ci}^2 c_{si}^2 \\ &\quad + \sum_{i=1}^{n-1} \sum_{j=i+1}^n (a_{ci}c_{sj} - a_{sj}c_{ci})^2 \\ \sum_{i=1}^n a_{si}^2 \sum_{i=1}^n c_{ci}^2 &= \sum_{i=1}^n a_{si}^2 c_{ci}^2 \\ &\quad + \sum_{i=1}^{n-1} \sum_{j=i+1}^n (a_{si}c_{cj} - a_{sj}c_{si})^2 \\ \sum_{i=1}^n a_{si}^2 \sum_{i=1}^n c_{si}^2 &= \sum_{i=1}^n a_{si}^2 c_{si}^2 \\ &\quad + \sum_{i=1}^{n-1} \sum_{j=i+1}^n (a_{si}c_{sj} - a_{sj}c_{si})^2. \end{aligned} \right. \quad (14)$$

The first item to the right of the equal sign is brought by $v_{ab}(t)$ and $i_z(t)$ with identical frequency while the second term is brought by $v_{ab}(t)$ and $i_z(t)$ with different frequencies.

The sum of the first items in (14) is given as

$$\begin{aligned} & \sum_{i=1}^n a_{ci}^2 c_{ci}^2 + \sum_{i=1}^n a_{ci}^2 c_{si}^2 + \sum_{i=1}^n a_{si}^2 c_{ci}^2 + \sum_{i=1}^n a_{si}^2 c_{si}^2 \\ &= \sum_{i=1}^n (a_{ci}^2 c_{ci}^2 + a_{si}^2 c_{si}^2) + \sum_{i=1}^n (a_{ci}^2 c_{si}^2 + a_{si}^2 c_{ci}^2) \\ &= P^2 + Q_B^2. \end{aligned} \quad (15)$$

The sum of the second items in (14) is denoted as D_B^2 , where

$$\begin{aligned} D_B^2 &= \sum_{i=1}^{n-1} \sum_{j=i+1}^n \left((a_{ci}^2 + a_{si}^2)(c_{cj}^2 + c_{sj}^2) \right. \\ &\quad \left. + 2 \sum_{i=1}^{n-1} \sum_{j=i+1}^n \left(a_{ci} a_{cj} c_{ci} c_{cj} + a_{si} a_{sj} c_{ci} c_{cj} \right. \right. \\ &\quad \left. \left. + a_{ci} a_{cj} c_{si} c_{sj} + a_{si} a_{sj} c_{si} c_{sj} \right) \right). \end{aligned} \quad (16)$$

In [2], there is $S_{ab}^2 = P^2 + Q_B^2 + D_B^2$, and D_B is termed as distortion power. Power factor PF_{ab} and PF_{cd} are given as $PF_{ab} = p_{ab0c}/S_{ab}$, $PF_{cd} = p_{cd0c}/S_{cd}$. PF_{ab} and PF_{cd} are used to estimate the power quality in the ac power system, but the meaning of PF_{ab} and PF_{cd} are vague in DAB due to the nonsinusoidal characteristic of HFL electric quantities. By comparison, S_{ab} and $p_{ab}(t)$ are inconsistent in the processing of power components with different frequencies. As for active power components generated by $v_{ab}(t)$ and $i_z(t)$ in-phase at the same frequency, S_{ab} treats them as a two-norm form, while $p_{ab}(t)$ treats them as arithmetic mean. As for nonactive power components generated by $v_{ab}(t)$ and $i_z(t)$ with different frequencies, S_{ab} treats them as square summation directly. However, discrete convolution and discrete correlation are adopted in $p_{ab}(t)$ to calculate the frequency sum and difference terms, respectively.

Because of this relationship between S_{ab} and $p_{ab}(t)$, it is difficult to separate a plurality of different power components from S_{ab} and correspond them to $p_{ab}(t)$ without overlapping or missing. Besides, as for a current component with a certain frequency, what kind of power it will produce is related to the voltage component with which it interacts. Hence, it is difficult to define whether a current component is an active current component or a nonactive current component.

In order to analyze power quality of HFL in DAB from $p_{ab}(t)$, two novel indicators are defined as follows:

$$\|p_{ab0c}\|_1 \triangleq \frac{|p_{ab0c}|}{\|p_{ab}(t)\|_1}, \|p_{ab0c}\|_2 \triangleq \frac{|p_{ab0c}|}{\|p_{ab}(t)\|_2}. \quad (17)$$

$\|p_{ab0c}\|_1$ and $\|p_{ab0c}\|_2$ are used to measure the dc component in $p_{ab}(t)$ from the perspective of signal strength and signal energy. From the perspective of $p_{cd}(t)$, $\|p_{cd0c}\|_1$, and $\|p_{cd0c}\|_2$ can be defined in similar way. Generally, the higher $\|p_{ab0c}\|_1$, $\|p_{ab0c}\|_2$, $\|p_{cd0c}\|_1$, and $\|p_{cd0c}\|_2$, the better performance of HFL, and the higher the efficiency of DAB.

III. HFL ANALYSIS OF DAB WITH MULTIPLE MODULATION SCHEMES

As shown in Fig. 2, DAB consists of four primary switches S_1 – S_4 , four secondary switches S_5 – S_8 , power transmission inductor

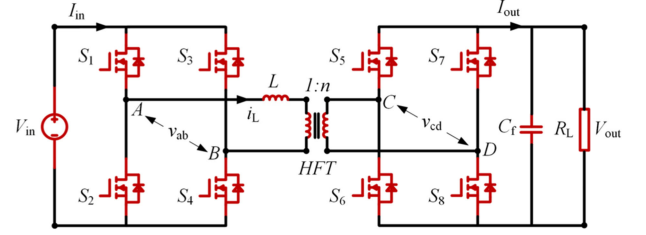


Fig. 2. Topology of DAB.

TABLE I
ABBREVIATIONS AND NORMALIZATIONS

Variable	Symbol	Normalized variable
Voltage base	V_{in}	-
Impedance	$Z = 2\pi f_s L$	-
Time/duration	t	$\theta = 2\pi f_s t$
Voltage gain	$M = V_o / nV_{in}$	-
Power base	$P = M\pi/4$	-

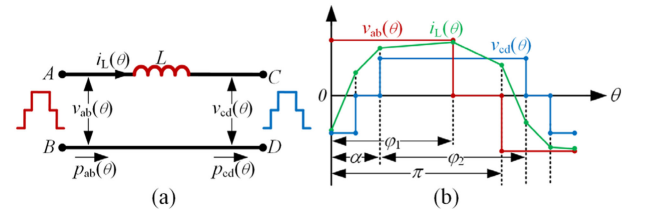


Fig. 3. (a) Simplified HFL of DAB with TPS. (b) Operation waveforms of DAB with TPS.

L , and high-frequency transformer (HFT). The ratio of HFT is 1: n and the switching frequency is f_s . Although some literature [48], [49] adopted variable switching frequency to improve the efficiency of DAB in some conditions, most DABs are with constant switching frequency for simple and practical purpose. V_{in} , V_{out} , I_{in} , and I_{out} denote the input voltage, output voltage, input current, and output current, respectively. The port voltage and inductor current are, respectively, denoted as v_{ab} , v_{cd} , and i_L .

In order to simplify the analysis, normalized values are used and summarized in Table I.

The phase-shift angle between two bridges α , duty ratios in primary bridge φ_1 , and secondary bridge φ_2 are expressed in radian, and the control coordinate is denoted as $(\alpha, \varphi_1, \varphi_2)$. The simplified HFL of DAB with TPS and corresponding operation waveforms are depicted in Fig. 3. The harmonic order of Fourier series is chosen as 5 for a clear analysis with a certain accuracy.

Multiple modulation schemes, including SPS, DPS, EPS, FOM, minimum I_{rms} modulation scheme, and ZCPM are analyzed and compared in this Section.

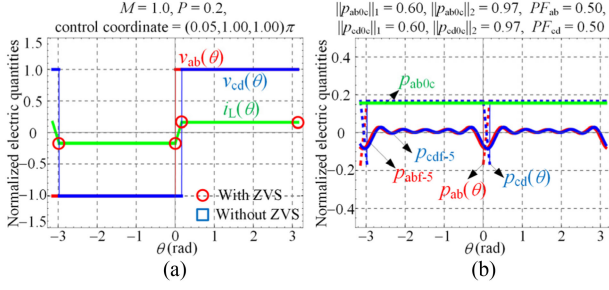


Fig. 4. Operation waveforms of SPS. (a) Waveforms of $v_{ab}(\theta)$, $v_{cd}(\theta)$, and $i_L(\theta)$ with $M = 1$, $P = 0.2$. (b) Waveforms of instantaneous power with $M = 1$, $P = 0.2$.

A. Single-Phase-Shift Modulation Scheme

SPS regulates α solely, while φ_1 and φ_2 are fixed to π . According to the value of M , SPS is divided into voltage match condition ($M = 1$) and voltage mismatch condition ($M \neq 1$).

1) *Voltage Match Condition of DAB With SPS*: Operation waveforms of SPS with $M = 1$, $P = 0.2$ is depicted in Fig. 4, and the control coordinate is $(0.05, 1.00, 1.00)\pi$. The red, blue, and green lines in Fig. 4(a) denote $v_{ab}(\theta)$, $v_{cd}(\theta)$, and $i_L(\theta)$, respectively. The red circle and blue square represent whether the zero-voltage-switching (ZVS) implementation of switches is achieved. In Fig 4(b), the dashed red and blue lines denote instantaneous power $p_{ab}(\theta)$ and $p_{cd}(\theta)$. The solid red and blue lines denote the fifth-order Fourier reconstruction of fluctuation power p_{abf} and p_{cdf} , which are calculated with (8)–(10) and denoted as p_{abf-5} and p_{cdf-5} , respectively. The green line denotes dc power p_{ab0c} (also equals to p_{cd0c}). The circulating power of $p_{ab}(\theta)$ and $p_{cd}(\theta)$ are the negative part of $p_{ab}(\theta)$ and $p_{cd}(\theta)$, which are denoted as p_{abc} and p_{cdc} [not illustrated in Fig 4(b)].

When $M = 1$, $P = 0.2$, ZVS for all switches can be achieved. The fifth-order Fourier decomposition of $v_{ab}(\theta)$, $v_{cd}(\theta)$, $i_L(\theta)$, and instantaneous power $p_{ab}(\theta)$ and $p_{cd}(\theta)$ are given as

$$\begin{cases} v_{ab}(\theta) \approx 1.27\sin(\theta) + 0.42\sin(3\theta) + 0.25\sin(5\theta) \\ v_{cd}(\theta) \approx 1.26\sin(\theta) + 0.38\sin(3\theta) + 0.18\sin(5\theta) \\ \quad - 0.20\cos(\theta) - 0.19\cos(3\theta) - 0.18\cos(5\theta) \\ i_L(\theta) \approx 0.20\sin(\theta) + 0.06\sin(3\theta) + 0.04\sin(5\theta) \\ \quad - 0.02\cos(\theta) - 0.02\cos(3\theta) - 0.01\cos(5\theta) \\ p_{ab}(\theta) \approx 0.16 - 0.02\cos(2\theta) - 0.02\cos(4\theta) \\ \quad - 0.02\cos(6\theta) - 0.02\cos(8\theta) - 0.01\cos(10\theta) \\ p_{cd}(\theta) \approx 0.16 - 0.02\cos(2\theta) - 0.02\cos(4\theta) \\ \quad - 0.02\cos(6\theta) - 0.02\cos(8\theta) - 0.01\cos(10\theta). \end{cases} \quad (18)$$

The sine terms of $p_{ab}(\theta)$ and $p_{cd}(\theta)$ are smaller than 0.01 and are neglected in (18). Hence, the HFL quantities are given as

$$\mathbf{v}_{abs} \approx [1.27, 0, 0.42, 0, 0.25]^T$$

$$\mathbf{v}_{abc} = 0,$$

$$\mathbf{v}_{cds} \approx [1.26, 0, 0.38, 0, 0.18]^T$$

$$\mathbf{v}_{cdc} \approx [-0.20, 0, 0.19, 0, 0.18]^T$$

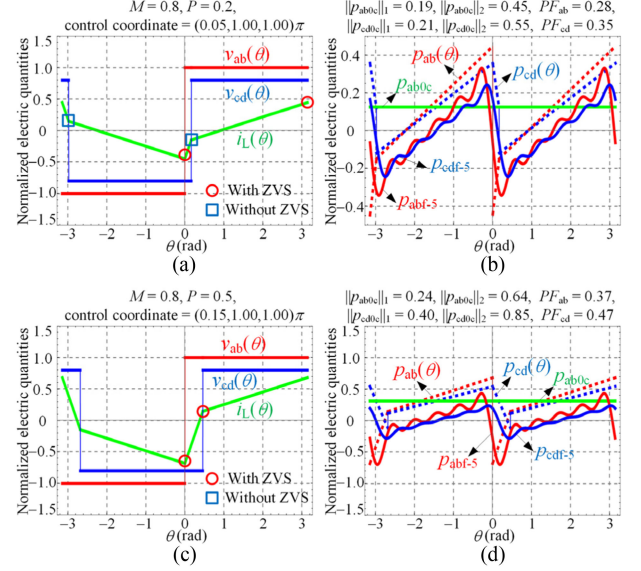


Fig. 5. Operation waveforms of SPS. (a) Waveforms of $v_{ab}(\theta)$, $v_{cd}(\theta)$, and $i_L(\theta)$ with $M = 0.8$, $P = 0.2$. (b) Waveforms of instantaneous power with $M = 0.8$, $P = 0.2$. (c) Waveforms of $v_{ab}(\theta)$, $v_{cd}(\theta)$, and $i_L(\theta)$ with $M = 0.8$, $P = 0.5$. (d) Waveforms of instantaneous power with $M = 0.8$, $P = 0.5$.

$$\mathbf{i}_{zs} \approx [0.20, 0, 0.06, 0, 0.04]^T$$

$$\mathbf{i}_{zc} \approx [-0.02, 0, 0.02, 0, 0.01]^T. \quad (19)$$

Indicators $\|p_{ab0c}\|_1$, $\|p_{ab0c}\|_2$, $\|p_{cd0c}\|_1$, $\|p_{cd0c}\|_2$, PF_{ab} , and PF_{cd} are given as

$$\|p_{ab0c}\|_1 \approx 0.60, \|p_{ab0c}\|_2 \approx 0.97, PF_{ab} \approx 0.50$$

$$\|p_{cd0c}\|_1 \approx 0.60, \|p_{cd0c}\|_2 \approx 0.97, PF_{cd} \approx 0.50. \quad (20)$$

The indicators for $p_{ab}(\theta)$ is the same as that for $p_{cd}(\theta)$ when $M = 1$, due to the symmetric characteristic of DAB and they are all with high values.

2) *Voltage Mismatch Condition of DAB With SPS*: Operation waveforms of SPS with $M = 0.8$, $P = 0.2$ and $M = 0.8$, $P = 0.5$ are depicted in Fig. 5.

When $M = 0.8$, $P = 0.2$, ZVS is only achieved for primary switches while the secondary switches suffer from hard switching. The HFL quantities and indicators are given as

$$\mathbf{v}_{abs} \approx [1.27, 0, 0.42, 0, 0.25]^T$$

$$\mathbf{v}_{abc} = 0$$

$$\mathbf{v}_{cds} \approx [1.00, 0, 0.30, 0, 0.14]^T$$

$$\mathbf{v}_{cdc} \approx [-0.16, 0, 0.15, 0, 0.14]^T$$

$$\mathbf{i}_{zs} \approx [0.16, 0, 0.05, 0, 0.01]^T$$

$$\mathbf{i}_{zc} \approx [-0.27, 0, 0.04, 0, 0.02]^T \quad (21)$$

$$\|p_{ab0c}\|_1 \approx 0.19, \|p_{ab0c}\|_2 \approx 0.45, PF_{ab} \approx 0.28$$

$$\|p_{cd0c}\|_1 \approx 0.21, \|p_{cd0c}\|_2 \approx 0.55, PF_{cd} \approx 0.35. \quad (22)$$

From (19) and (21), c_{c1} (the first term of \mathbf{i}_{zc}) when $M < 1$ is much greater than that when $M = 1$ and it resulted in large p_{abc} ,

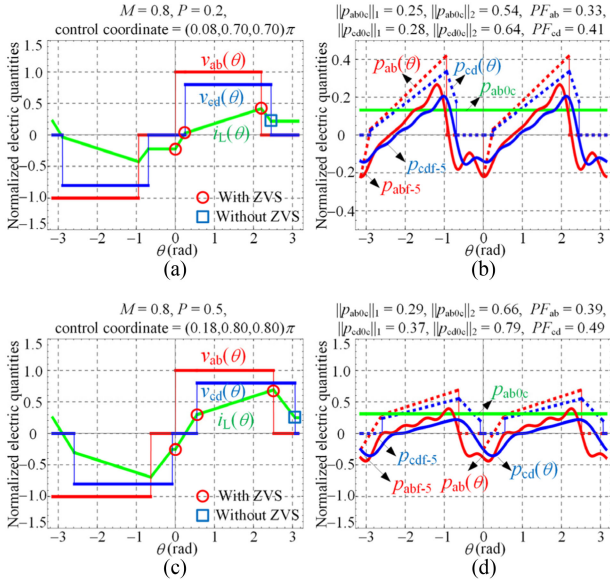


Fig. 6. Operation waveforms of DPS. (a) Waveforms of $v_{ab}(\theta)$, $v_{cd}(\theta)$, and $i_L(\theta)$ with $M = 0.8$, $P = 0.2$. (b) Waveforms of instantaneous power with $M = 0.8$, $P = 0.2$. (c) Waveforms of $v_{ab}(\theta)$, $v_{cd}(\theta)$, and $i_L(\theta)$ with $M = 0.8$, $P = 0.5$. (d) Waveforms of instantaneous power with $M = 0.8$, $P = 0.5$.

p_{cdc} and low indicators. Similar conclusions can also be drawn when $M > 1$. With the increasing of P , the ZVS implementation for secondary switches is achieved in Fig. 5(c), and all indicators are improved in Fig. 5(d).

B. Dual-Phase-Shift Modulation Scheme

DPS was proposed in [34] to reduce circulating power and increase efficiency in low power conditions. Operation waveforms when $M = 0.8$, $P = 0.2$, and $M = 0.8$, $P = 0.5$ with DPS are depicted in Fig. 6.

In Fig. 6(a), the HFL quantities and indicators are given as

$$\begin{aligned} \mathbf{v}_{abs} &\approx [1.01, 0, 0.01, 0, 0.12]^T \\ \mathbf{v}_{abc} &= [0.51, 0, 0.06, 0, -0.12]^T \\ \mathbf{v}_{cds} &\approx [0.88, 0, 0.04, 0, 0.06]^T \\ \mathbf{v}_{cdc} &\approx [0.21, 0, 0.03, 0, -0.13]^T \\ \mathbf{i}_{zs} &\approx [0.30, 0, 0.01, 0, 0.01]^T \\ \mathbf{i}_{zc} &\approx -[0.13, 0, 0.01, 0, 0.03]^T \end{aligned} \quad (23)$$

$$\begin{aligned} \|p_{ab0c}\|_1 &\approx 0.25, \|p_{ab0c}\|_2 \approx 0.54, PF_{ab} \approx 0.33 \\ \|p_{cd0c}\|_1 &\approx 0.28, \|p_{cd0c}\|_2 \approx 0.64, PF_{cd} \approx 0.41. \end{aligned} \quad (24)$$

From (21) to (24), p_{abf} in DPS is greatly reduced and all indicators are improved compared with SPS when $M = 0.8$, $P = 0.2$. Besides, two secondary switches are with hard switching. As for DPS in medium power conditions in Fig. 6(c) and (d), the ZVS implementation as well as all indicators are deteriorated compared with SPS.

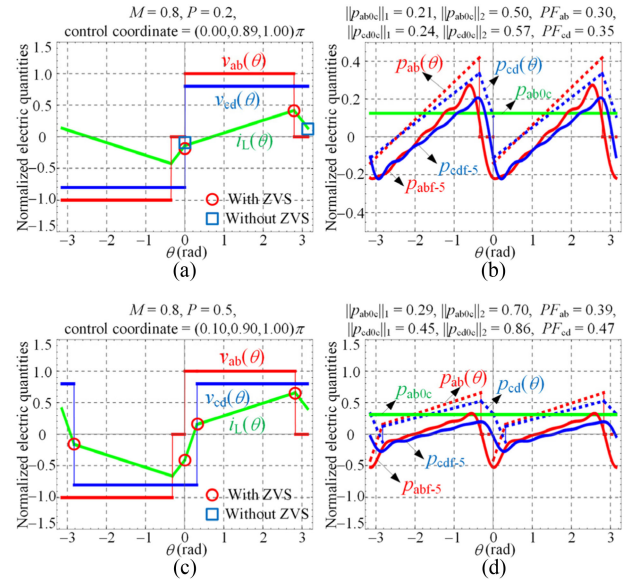


Fig. 7. Operation waveforms of EPS. (a) Waveforms of $v_{ab}(\theta)$, $v_{cd}(\theta)$, and $i_L(\theta)$ with $M = 0.8$, $P = 0.2$. (b) Waveforms of instantaneous power with $M = 0.8$, $P = 0.2$. (c) Waveforms of $v_{ab}(\theta)$, $v_{cd}(\theta)$, and $i_L(\theta)$ with $M = 0.8$, $P = 0.5$. (d) Waveforms of instantaneous power with $M = 0.8$, $P = 0.5$.

C. Extended-Phase-Shift Modulation Scheme

EPS was proposed in [10] to eliminate circulating power in medium power conditions. Operation waveforms when $M = 0.8$, $P = 0.2$ and $M = 0.8$, $P = 0.5$ with DPS are depicted in Fig. 7.

In Fig. 7, the control coordinate of EPS is very close to SPS. Hence, they are with similar ZVS implementation and close indicators.

D. Fundamental-Optimal Modulation Scheme

FOM was proposed in [25] to maximize fundamental active power generated by voltage and current with the fundamental frequency. Operation waveforms when $M = 0.8$, $P = 0.2$ and $M = 0.8$, $P = 0.5$ with FOM are depicted in Fig. 8.

In Fig. 8, φ_1 with FOM is smaller than that with the other modulation schemes. Hence, FOM is with higher PF_{ab} because fundamental active power is maximized. However, the ZVS implementation of FOM is not good compared with DPS in low power conditions and EPS in medium power conditions.

E. Minimum I_{rms} Modulation Scheme

The minimum I_{rms} modulation scheme chooses I_{rms} as the optimization objective, and the operation region is divided into low, medium, and high power regions.

A detailed region and control coordinate calculation is presented in [30], [31]. Operation waveforms when $M = 0.8$, $P = 0.2$ and $M = 0.8$, $P = 0.5$ with minimum I_{rms} modulation scheme are depicted in Fig. 9.

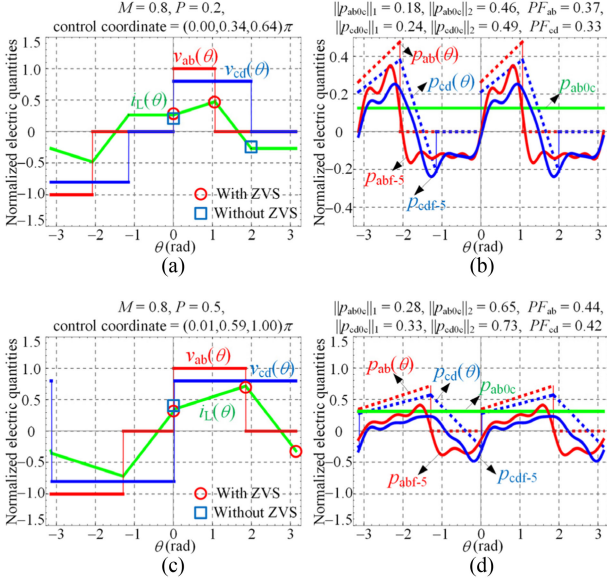


Fig. 8. Operation waveforms of FOM. (a) Waveforms of $v_{ab}(\theta)$, $v_{cd}(\theta)$, and $i_L(\theta)$ with $M = 0.8$, $P = 0.2$. (b) Waveforms of instantaneous power with $M = 0.8$, $P = 0.2$. (c) Waveforms of $v_{ab}(\theta)$, $v_{cd}(\theta)$, and $i_L(\theta)$ with $M = 0.8$, $P = 0.5$. (d) Waveforms of instantaneous power with $M = 0.8$, $P = 0.5$.

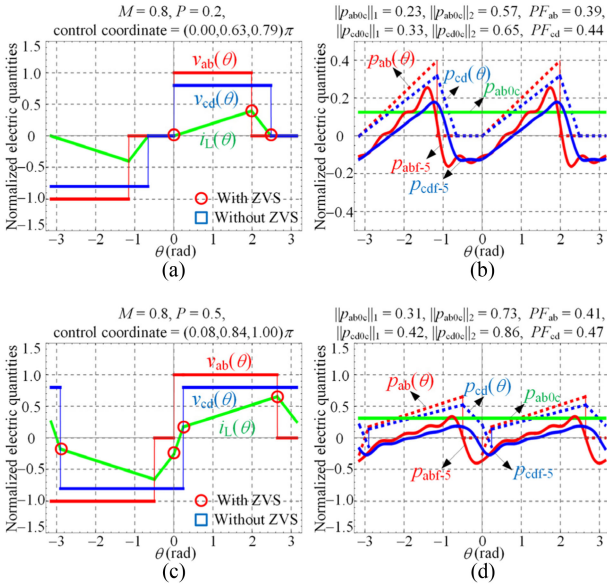


Fig. 9. Operation waveforms of minimum I_{rms} modulation scheme. (a) Waveforms of $v_{ab}(\theta)$, $v_{cd}(\theta)$, and $i_L(\theta)$ with $M = 0.8$, $P = 0.2$. (b) Waveforms of instantaneous power with $M = 0.8$, $P = 0.2$. (c) Waveforms of $v_{ab}(\theta)$, $v_{cd}(\theta)$, and $i_L(\theta)$ with $M = 0.8$, $P = 0.5$. (d) Waveforms of instantaneous power with $M = 0.8$, $P = 0.5$.

In Fig. 9(a), when $M = 0.8$, $P = 0.2$, ZVS for all switches are achieved. The HFL quantities and indicators are given as

$$\begin{aligned} \mathbf{v}_{abs} &\approx [0.89, 0, 0.01, 0, 0.24]^T \\ \mathbf{v}_{abc} &\approx [0.58, 0, -0.07, 0, 0.06]^T \\ \mathbf{v}_{cds} &\approx [0.91, 0, 0.10, 0, 0.01]^T \end{aligned}$$

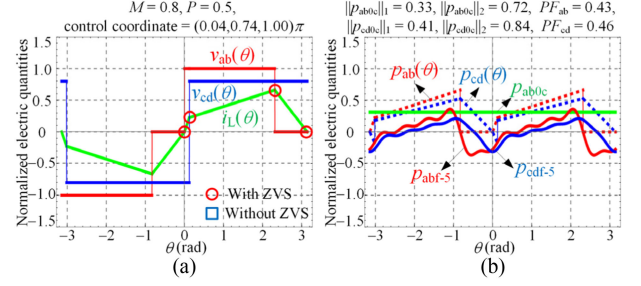


Fig. 10. Operation waveforms of ZCPM. (a) Waveforms of $v_{ab}(\theta)$, $v_{cd}(\theta)$, and $i_L(\theta)$ with $M = 0.8$, $P = 0.5$. (b) Waveforms of instantaneous power with $M = 0.8$, $P = 0.5$.

$$\begin{aligned} \mathbf{v}_{cdc} &\approx [0.31, 0, 0.16, 0, -0.02]^T \\ \mathbf{i}_{zs} &\approx [0.27, 0, -0.07, 0, 0.01]^T \\ \mathbf{i}_{zc} &\approx [0.02, 0, 0.03, 0, -0.05]^T \end{aligned} \quad (25)$$

$$\begin{aligned} \|p_{ab0c}\|_1 &\approx 0.23, \|p_{ab0c}\|_2 \approx 0.57, PF_{ab} \approx 0.39 \\ \|p_{cd0c}\|_1 &\approx 0.33, \|p_{cd0c}\|_2 \approx 0.65, PF_{cd} \approx 0.44. \end{aligned} \quad (26)$$

p_{abc} and p_{cdc} are both zero. Besides, $i_L(\theta)$ remains zero when $v_{ab}(\theta)$ and $v_{cd}(\theta)$ are both zero. When the operation range is out of the low power region, the above two conditions cannot be satisfied simultaneously. As for minimum I_{rms} modulation scheme in medium power region depicted in Fig. 9(c) and (d), both p_{abc} and p_{cdc} are nonzero. The control coordinate in high power region is the same as SPS, and the analysis is presented in the first part of this section.

F. Zero Circulating Power Modulation Scheme

ZCPM aims to eliminate p_{abc} . It is obvious that minimum I_{rms} modulation scheme in low power region belongs to ZCPM. Operation waveforms when $M = 0.8$, $P = 0.5$ with ZCPM is depicted in Fig. 10. In Fig. 10(a), ZVS implementation for all switches is achieved. Although ZCPM is with 1.5% higher I_{rms} compared with minimum I_{rms} modulation scheme, S_{ab} with ZCPM is 11% smaller than that with minimum I_{rms} modulation scheme. Hence, ZCPM is with higher PF_{ab} and smaller p_{abf} due to a shrinking φ_1 .

IV. COMPARISON ANALYSIS AND MULTIINDICATOR EVALUATION AND OPTIMIZATION OF DAB

A comparison of the modulation schemes mentioned above is made in this section, and a multiindicator evaluation and optimization for DAB is established to enhance the efficiency of DAB.

A. Comparison of Modulation Schemes

Eight indicators are adopted to compare the modulation schemes mentioned above. PF_{ab} , $\|p_{ab0c}\|_1$, and $\|p_{ab0c}\|_2$ are indicators from $p_{ab}(\theta)$. PF_{cd} , $\|p_{cd0c}\|_1$, and $\|p_{cd0c}\|_2$ are indicators from $p_{cd}(\theta)$. I_{rms} and ZVS are adopted to estimate the conduction and switching loss of DAB. ZVS = 1 indicates that

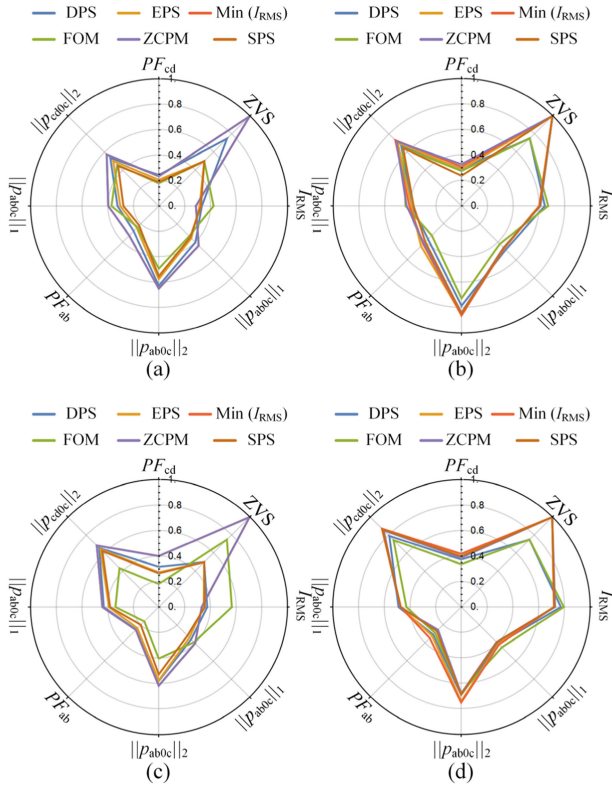


Fig. 11. Indicators comparison with multiple modulation schemes. (a) $M = 0.8$, $P = 0.2$. (b) $M = 0.8$, $P = 0.5$. (c) $M = 1.2$, $P = 0.2$. (d) $M = 1.2$, $P = 0.5$.

all switches are with ZVS implementation, while $ZVS = 0.75$ indicates six out of eight switches are with ZVS implementation. Multiple modulation schemes mentioned above when $M = 0.8$, $P = 0.2$, $M = 0.8$, $P = 0.5$, $M = 1.2$, $P = 0.2$, and $M = 1.2$, $P = 0.5$ are compared and the results are illustrated in Fig. 11. In Fig. 11(a) and (c), when M and P are both away from unity, minimum I_{rms} modulation scheme and ZCPM are with the same control coordinate. Most of the modulation schemes cannot achieve ZVS for all switches except for minimum I_{rms} modulation scheme (also ZCPM). The differences of all indicators with multiple modulation schemes are obvious. All indicators reach the maximum with minimum I_{rms} modulation scheme (also ZCPM), while SPS is with the smallest indicators. With the increasing of P in Fig. 11(b) and (d), the ZVS implementation for all switches becomes easier to achieve, and the differences of all indicators with multiple modulation schemes are tiny.

The instantaneous power spectrum with multiple modulation schemes mentioned above when $M = 0.8$, $P = 0.2$, $M = 0.8$, $P = 0.5$, $M = 1.2$, $P = 0.2$, and $M = 1.2$, $P = 0.5$ are compared in Fig. 12. In Fig. 12, the first column represents p_{ab0c} and p_{cd0c} , while the other columns represent p_{abf} and p_{cdf} with different frequencies.

Because $v_{ab}(\theta)$, $v_{cd}(\theta)$, and $i_L(\theta)$ only contain odd harmonic components, p_{abf} and p_{cdf} only contain even harmonic components. In Fig. 12(a) and (c), p_{abf} and p_{cdf} reach the minimum with minimum I_{rms} modulation scheme (also ZCPM) in all harmonic frequencies. Therefore, all indicators reach the highest compared

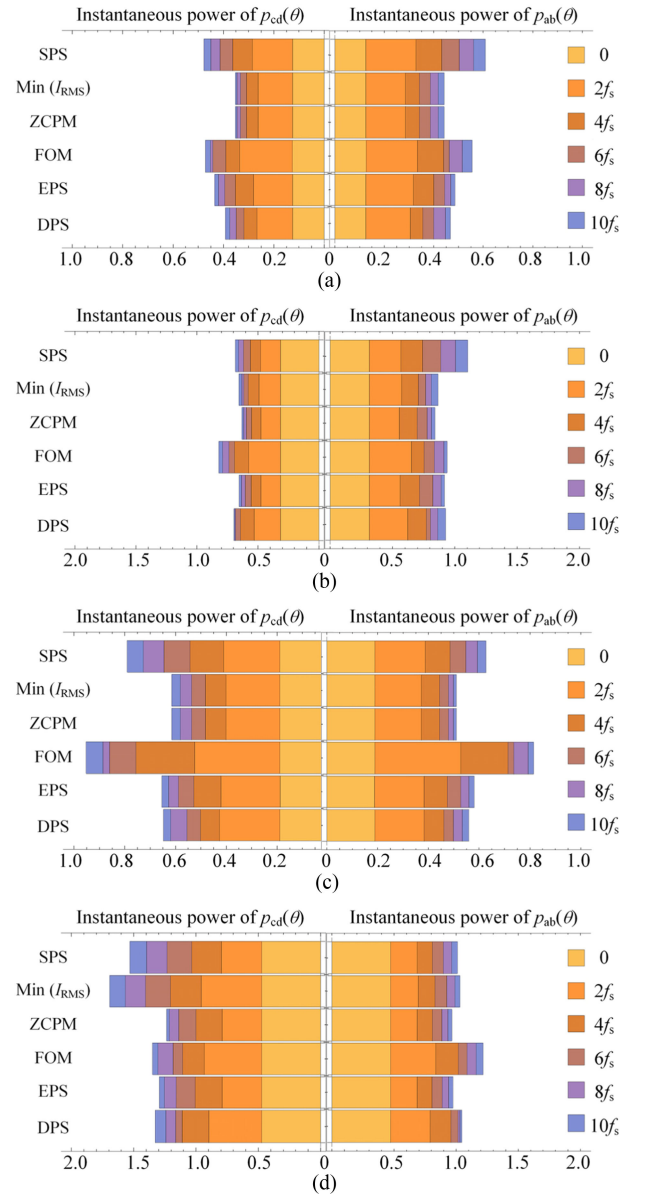


Fig. 12. Instantaneous power spectrum comparison with multiple modulation schemes. (a) $M = 0.8$, $P = 0.2$. (b) $M = 0.8$, $P = 0.5$. (c) $M = 1.2$, $P = 0.2$. (d) $M = 1.2$, $P = 0.5$.

to the other modulation schemes. SPS and EPS are with higher p_{abf} and p_{cdf} . In Fig. 12(b) and (d), the amplitude of p_{abf} and p_{cdf} does not reach the minimum with one certain modulation scheme in all harmonic frequencies. EPS is with the minimum p_{abf} , while DPS is with the minimum p_{cdf} . However, the differences of p_{abf} and p_{cdf} for multiple modulation schemes when $P = 0.5$ are smaller than that when $P = 0.2$.

In the low power region of minimum I_{rms} modulation scheme, minimum I_{rms} modulation scheme (also ZCPM) are recommended because of minimum I_{rms} , zero p_{abc} and p_{cdc} , and full ZVS implementation. DPS is also recommended when P is not too small for simpler implementation. Out of the range of low power region of minimum I_{rms} modulation scheme, minimum I_{rms} and zero p_{abc} or p_{cdc} cannot be satisfied simultaneously. Meanwhile, all indicators will not reach the minimum

with one certain modulation scheme. Minimum I_{rms} modulation scheme and ZCPM are still recommended as they have an advantage in several indicators. However, the analytical expressions of minimum I_{rms} modulation scheme in the medium power region is complex and the digital implementation is difficult [30], [31]. When P is not too large, EPS is also recommended for simpler implementation. When P is large or when M is very close to unity, SPS is recommended for easy implementation and high efficiency.

B. Multiindicator Evaluation and Optimization of DAB

In order to give a good estimation of the efficiency of DAB, all indicators mentioned above need to be considered comprehensively, and the optimization objective A can be designed as

$$A = \lambda_1 \|p_{ab0c}\|_1 + \lambda_2 \|p_{ab0c}\|_2 + \lambda_3 \text{PF}_{ab} + \lambda_4 \|p_{cd0c}\|_1 + \lambda_5 \|p_{cd0c}\|_2 + \lambda_6 \text{PF}_{cd} + \lambda_7 \text{ZVS} \quad (27)$$

where λ_i , $i = 1, \dots, 7$ are positive weight factors of A ranged from 0 to 1. The weight factors can be fixed values for easier implementation or dynamic values with the changing of P and M . In order to determine these weight factors for peak efficiency, advanced algorithms like artificial neural network, and deep learning method can be adopted. However, more in-depth research of these advanced algorithms is out of the scope of this article, and this article uses fixed values $\lambda_1 = 0.2$, $\lambda_2 = 0.2$, $\lambda_3 = 0.1$, $\lambda_4 = 0.2$, $\lambda_5 = 0.2$, $\lambda_6 = 0.1$, and $\lambda_7 = 0.1$. λ_7 can be set as a larger value for CoolMOS or SiC MOSFET-based DAB because the ZVS implementation of CoolMOS or SiC MOSFET-based DAB have a stronger relation to the efficiency improvement, especially in high-power-density applications. To allow for a certain margin, sufficient negative current is required to discharge and charge the parasitic capacitor of the switches in practical ZVS implementation. For determining the optimal control coordinate of DAB, a hybrid optimization algorithm based on gradient descent method is proposed, and the procedure is depicted in Fig. 13.

In Fig. 13, the procedure starts from the predefined range of M and P , the iteration step for M and P , denoted as dM and dP , the optimization objective A , the iteration step for control coordinate ($d\alpha$, $d\varphi_1$, and $d\varphi_2$), and the learning rate β . In each iteration cycle of M and P , the region calculation is adopted to determine which region is available. The operation region is classified into low power region and high power region, where

$$\begin{aligned} \text{Low power region: } & (P \in [0, 2M(1-M)) \wedge M \in (0, 1)) \\ & \vee \left(P \in \left[0, \frac{2(M-1)}{M^2} \right] \wedge M \in [1, \infty) \right) \\ \text{High power region: } & (P \in [2M(1-M), 1) \wedge M \in (0, 1)) \\ & \vee \left(P \in \left[\frac{2(M-1)}{M^2}, 1 \right] \wedge M \in [1, \infty) \right). \end{aligned} \quad (28)$$

In the low power region, the minimum I_{rms} modulation scheme is adopted since all indicators and A have the maximum values. The control coordinate is with analytical expressions

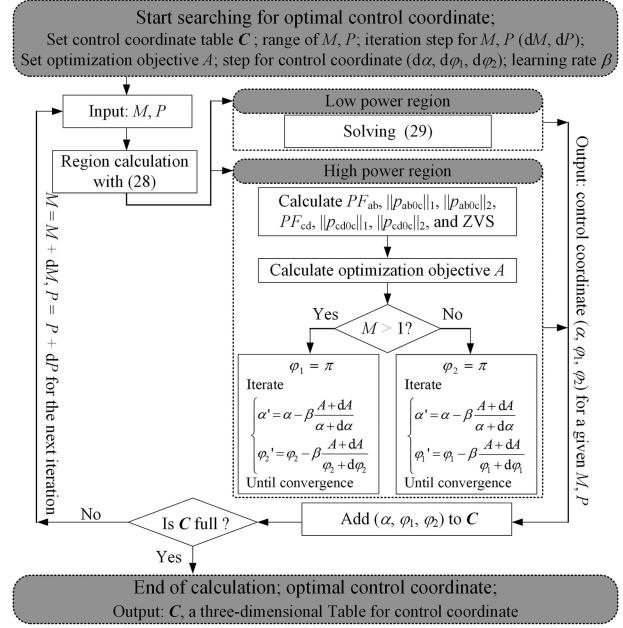


Fig. 13. Procedure to determine the optimal control coordinate based on gradient descent method.

[30], where

$$\begin{aligned} \alpha = 0, \varphi_1 &= \sqrt{\frac{MP}{2(1-M)}}\pi, \varphi_2 = \sqrt{\frac{P}{2M(1-M)}}\pi \\ &\forall P \in [0, 2M(1-M)) \wedge M \in (0, 1) \\ \alpha &= \sqrt{\frac{P(M-1)}{2}}\pi, \varphi_1 = \sqrt{\frac{M^2P}{2(M-1)}}\pi, \varphi_2 = \sqrt{\frac{P}{2(M-1)}}\pi \\ &\forall P \in \left[0, \frac{2(M-1)}{M^2} \right) \wedge M \in [1, \infty). \end{aligned} \quad (29)$$

In the high power region, the control coordinate is calculated by gradient descent method with initial values in SPS. Because the control coordinate of the upper bound of low power region is with $\varphi_1 = \pi$ when $M > 1$, and $\varphi_2 = \pi$ when $M < 1$, φ_1 and φ_2 remain the value in the high power region. Hence, there are two variables for iteration, and the iteration process is given as

$$\theta' = \theta - \beta \frac{A + dA}{\theta + d\theta}, \theta = \alpha, \varphi_1, \varphi_2. \quad (30)$$

Since a function has the largest rate of change along the gradient direction, we can achieve the optimization goal by reducing the function value along the negative gradient direction with (30). On repeating (30) until convergence and the optimal control coordinate is obtained. The learning rate β needs to be carefully selected. A higher β speeds up the optimization process but may cause oscillation around the minimum point. β is selected as 0.1 in the following cases. The maximum iteration number is set as 100, and the convergence condition is set as

$$|\theta' - \theta| < 0.01, \theta = \alpha, \varphi_1, \varphi_2. \quad (31)$$

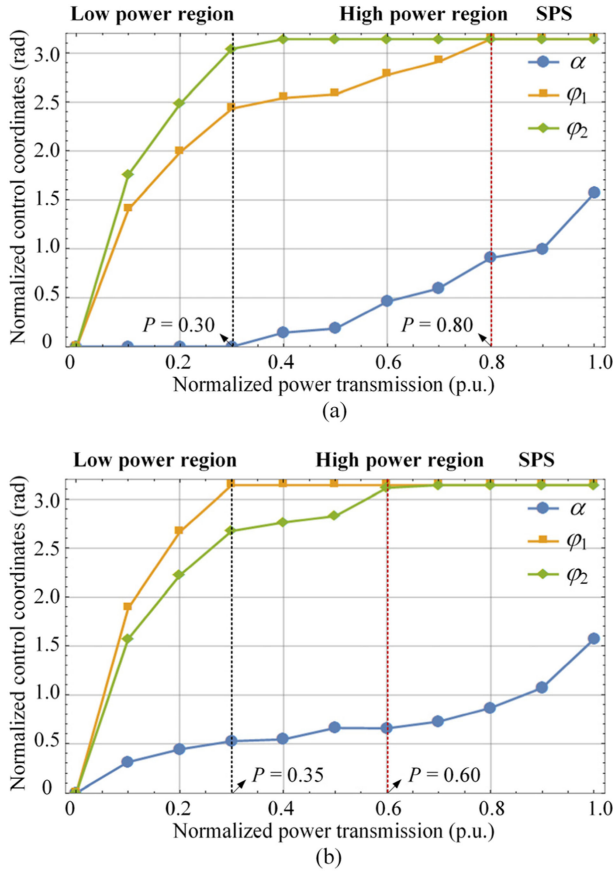


Fig. 14. Optimal control coordinate trajectories when (a) $M = 0.8$, (b) $M = 1.2$.

Once the optimal control coordinate is obtained with a given M and P , it will be added into the control coordinate table C . When C is not full, another iteration for M and P starts until M and P traverse through all the predefined range of M and P , and the optimal control coordinate in the predefined operation range in obtained.

With the procedure to determine the optimal control coordinate, the optimal control coordinate trajectories when $M = 0.8$ and $M = 1.2$ are depicted in Fig. 14.

In Fig. 14, when P is relatively high (beyond the red dashed line), the control coordinate is the same as SPS where $\varphi_1 = \varphi_2 = \pi$, which indicates that SPS is with the highest optimization objective A . The boundary of SPS in high power region when $M = 0.8$ and $M = 1.2$ are 0.80 and 0.60, respectively.

V. EXPERIMENTAL RESULTS

A laboratory prototype was built and the experimental results are presented in this section. The laboratory DAB prototype is depicted in Fig. 15, and the basic technical data of the prototype are listed below.

A laboratory prototype was built and the experimental results are presented in this section. The laboratory DAB prototype is depicted in Fig. 15 and the basic technical data of the prototype are listed as follows.

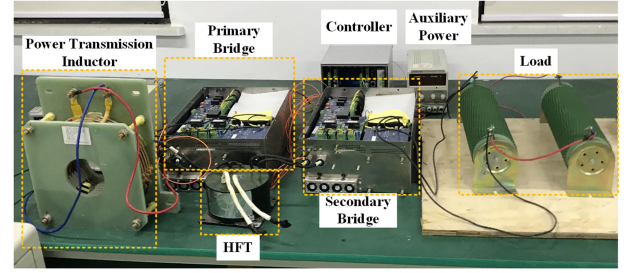


Fig. 15. Laboratory prototype of DAB.

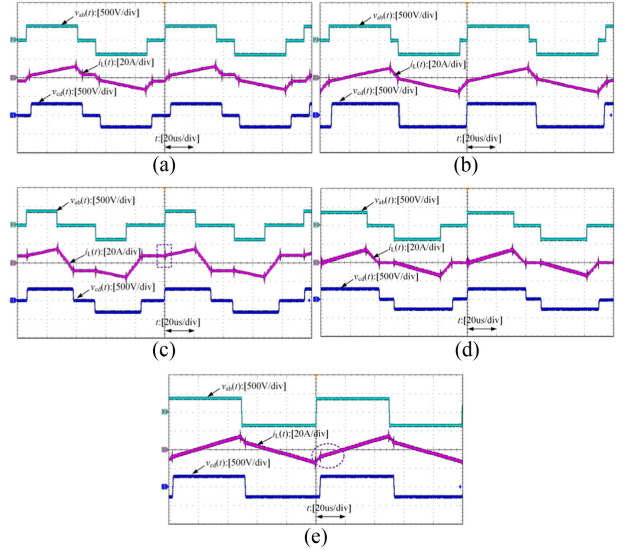


Fig. 16. Experimental waveforms in buck mode with low power. (a) DPS. (b) EPS. (c) FOM. (d) Minimum I_{rms} modulation scheme (ZCPM, also proposed optimal control coordinate). (e) SPS.

- 1) Primary/secondary side
 - a) DC capacitor: 380 $\mu\text{F}/900$ V, MKP film capacitors.
 - b) Switches: 2 IGBT module FF150R12MS4G.
- 2) High frequency transformer:
 - a) Turn ratio: 1:1.
 - b) Material: Nanocrystalline.
 - c) Leakage inductor: 10 μH .
- 3) Power transmission inductor: Air core coil, 247 μH .
- 4) Input voltage: 400 V, Output voltage: 320–480 V.
- 5) Switching frequency: 10 kHz.
- 6) Controller: DSP TMS320F28335.

The modulation schemes mentioned above are tested and compared in buck mode with low power [$V_{in} = 400$ V, $V_{out} = 320$ V, output power 1.6 kW ($P = 0.2$)], buck mode with medium power [$V_{in} = 400$ V, $V_{out} = 320$ V, output power 4.0 kW ($P = 0.5$)], boost mode with low power [$V_{in} = 400$ V, $V_{out} = 480$ V, output power 2.4 kW ($P = 0.2$)], and boost mode with medium power [$V_{in} = 400$ V, $V_{out} = 480$ V, output power 6.0 kW ($P = 0.5$)]. The operation waveforms are depicted in Figs. 16–19. The control coordinate, I_{rms} , and I_{Peak} are measured. Indicators PF_{ab} , $\|p_{ab0c}\|_1$, $\|p_{ab0c}\|_2$, PF_{cd} , $\|p_{cd0c}\|_1$, and $\|p_{cd0c}\|_2$, and the efficiency are estimated from the experimental data.

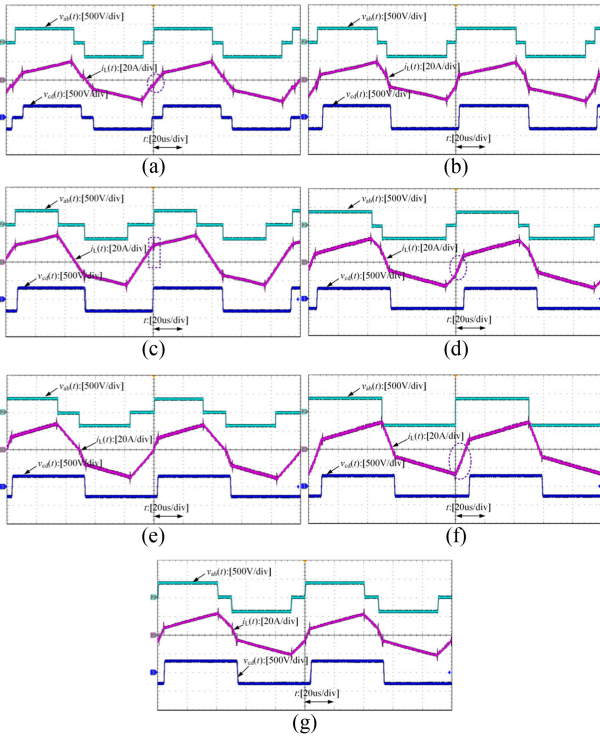


Fig. 17. Experimental waveforms in buck mode with medium power. (a) DPS. (b) EPS. (c) FOM. (d) Minimum I_{rms} modulation scheme. (e) ZCPM. (f) SPS. (g) Proposed optimal control coordinate.

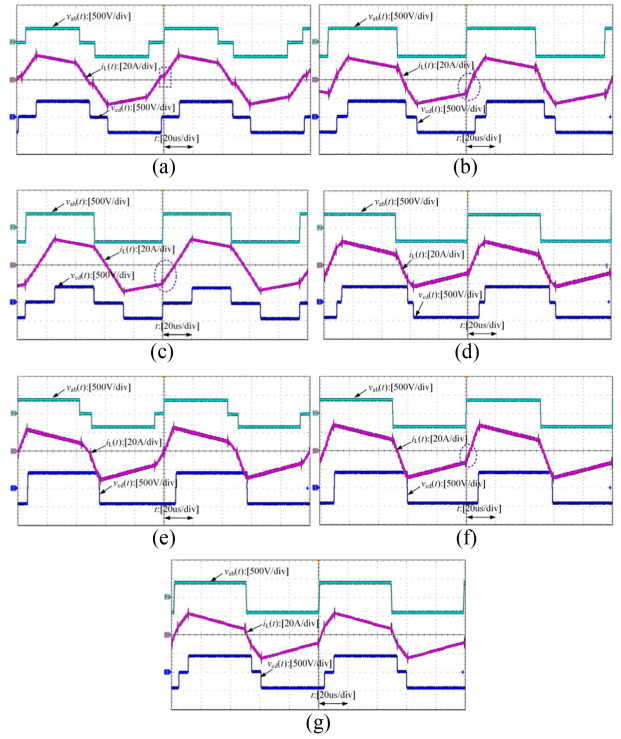


Fig. 19. Experimental waveforms in boost mode with medium power. (a) DPS. (b) EPS. (c) FOM. (d) Minimum I_{rms} modulation scheme. (e) ZCPM. (f) SPS. (g) Proposed optimal control coordinate.

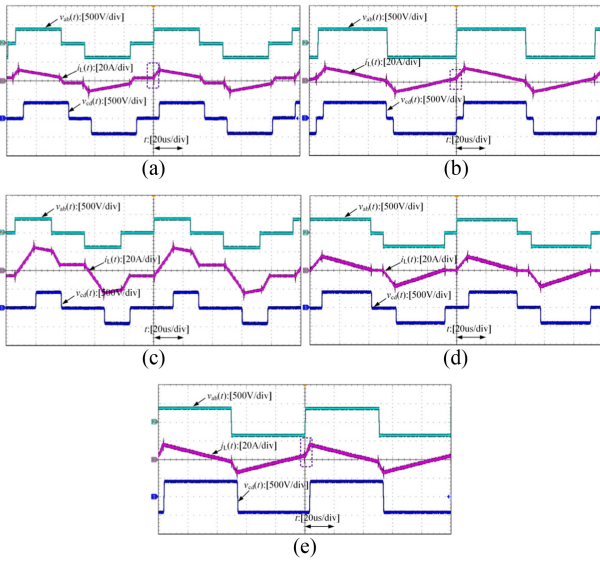


Fig. 18. Experimental waveforms in boost mode with low power. (a) DPS. (b) EPS. (c) FOM. (d) Minimum I_{rms} modulation scheme (ZCPM, also proposed optimal control coordinate). (e) SPS.

A. Operation Waveforms

1) *Buck Mode With Low Power*: In Fig. 16, FOM is with hard switching, and i_L remains a large value when v_{ab} and v_{cd} are both zero. EPS and DPS are with a little circulating power.

SPS is with larger circulating power and minimum I_{rms} modulation scheme (ZCPM, also the proposed optimal control coordinate) is with zero circulating power.

2) *Buck Mode With Medium Power*: In Fig. 17, FOM is still with hard switching and SPS is still with larger circulating power. Except for FOM, SPS, and EPS, DPS, minimum I_{rms} modulation scheme, ZCPM, and the proposed optimal control coordinate are with close control coordinate.

3) *Boost Mode With Low Power*: In Fig. 18, DPS, EPS, and SPS are with hard switching. FOM is with small circulating power while minimum I_{rms} modulation scheme (ZCPM, also the proposed optimal control coordinate) is with zero circulating power.

4) *Boost Mode With Medium Power*: In Fig. 19, DPS is still with hard switching and FOM is with larger circulating power. Except for DPS and FOM, EPS, SPS, minimum I_{rms} modulation scheme, ZCPM, and the proposed optimal control coordinate are with close control coordinate.

A comparison of I_{rms} and I_{Peak} with modulation schemes mentioned above is depicted in Fig. 20. In Fig. 20, when $P = 0.2$, FOM is with the highest I_{rms} and I_{Peak} . Minimum I_{rms} modulation scheme, ZCPM, and the proposed the proposed optimal control coordinate are identical and are with the minimum I_{rms} and I_{Peak} . When $P = 0.5$, minimum I_{rms} modulation scheme achieves minimum I_{rms} and the proposed optimal control coordinate is with the minimum I_{Peak} . However, the differences of I_{rms} and I_{Peak} are tiny due to very close control coordinate.

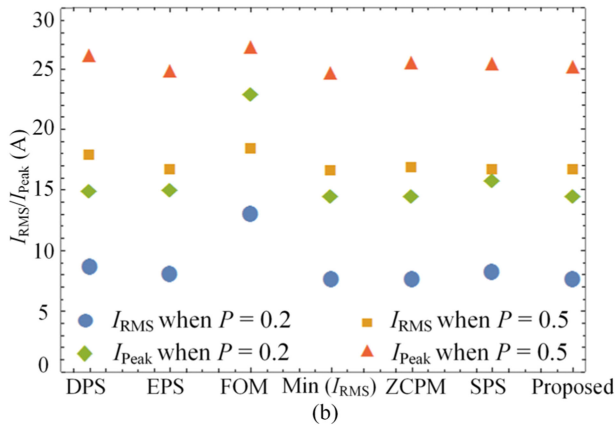
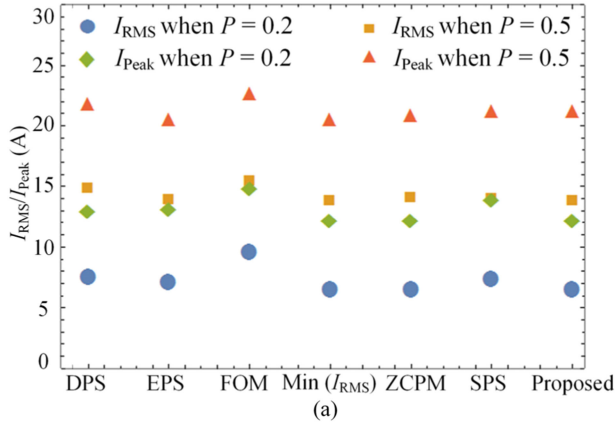


Fig. 20. I_{RMS} and I_{Peak} comparison with multiple modulation schemes. (a) $M = 0.8$. (b) $M = 1.2$.

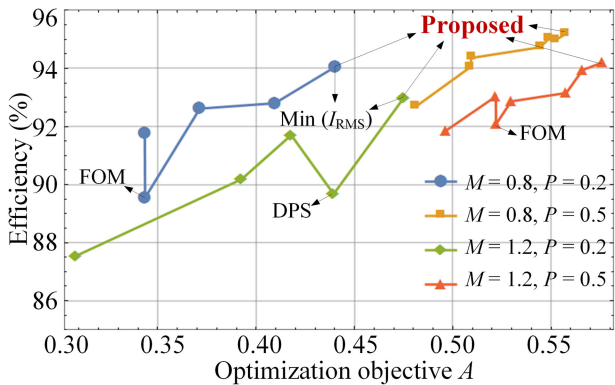


Fig. 21. Optimization objective A versus efficiency with multiple modulation schemes.

Fig. 21 shows the relation of optimization objective A and the efficiency of DAB. In general, A is proportional to efficiency except for some individual cases for FOM when $M = 0.8$, $P = 0.2$, DPS when $M = 1.2$, $P = 0.2$, and FOM when $M = 1.2$, $P = 0.5$. The major reason for this phenomenon is hard switching in these cases. Peak efficiency is achieved with the proposed optimal control coordinate by maximizing the optimization objective A . When different weight factors are

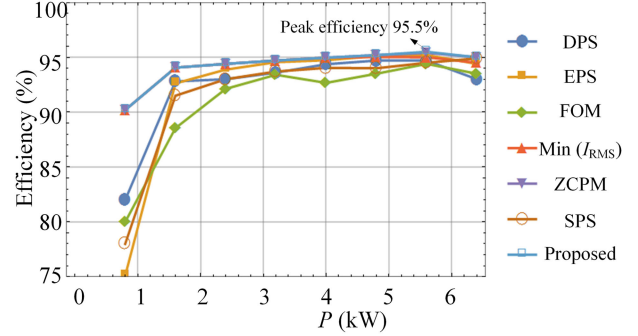


Fig. 22. Efficiency curves with multiple modulation schemes.

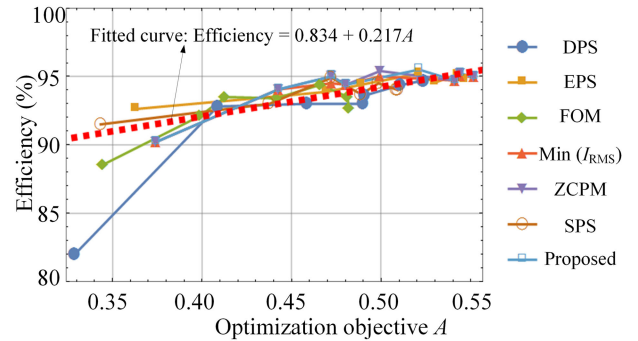


Fig. 23. Optimization objective A versus efficiency with multiple modulation schemes.

adopted, the optimization result is different but the efficiency differences are tiny.

B. Efficiency Curves and Effectiveness of Proposed Optimal Control Coordinate

The efficiency curves of multiple modulation schemes mentioned above when $V_{in} = 400$ V, $V_{out} = 320$ V, output power ranged from 0.8 to 6.4 kW are depicted in Fig. 22.

For various power transmission conditions, the efficiency with the proposed optimal control coordinate is higher than the other modulation schemes for most of the operation points, especially when $P \ll 2$ kW. When the power transmission is 0.8 kW, the efficiency of the proposed optimal control coordinate (also ZCPM and minimum I_{RMS} modulation scheme) is 90.2%, which is 17% higher than that with SPS, 14% higher than that with EPS, 11% higher than that with FOM, and also 9% higher than that with DPS. The peak efficiency of the prototype when $V_{in} = 400$ V, $V_{out} = 320$ V is 95.5% at 5.6-kW output power with the proposed optimal control coordinate, which is 1% higher than that with minimum I_{RMS} modulation scheme, and 2% higher than that with FOM. With the increasing of P , the efficiency differences of all modulation schemes become smaller. Except for FOM, all the efficiency curves of the other modulation schemes almost coincide when $P > 4$ kW because the control coordinates are very close.

The optimization objective A versus efficiency curve when $M = 0.8$ is depicted in Fig. 23.

TABLE II
COMPARISON OF INDICATORS VERSUS EFFICIENCY CURVES

Indicators	Error-avg	Standard error	T-statistic	P-value
PF_{ab}	0.024	0.136	1.649	1.1e-1
$\ p_{ab0c}\ _1$	0.020	0.070	9.884	1.0e-13
$\ p_{ab0c}\ _2$	0.016	0.026	13.375	8.9e-19
PF_{cd}	0.015	0.048	10.839	3.7e-15
$\ p_{cd0c}\ _1$	0.018	0.040	12.784	5.8e-18
$\ p_{cd0c}\ _2$	0.016	0.021	12.246	3.3e-17
A	0.007	0.020	24.167	1.2e-30

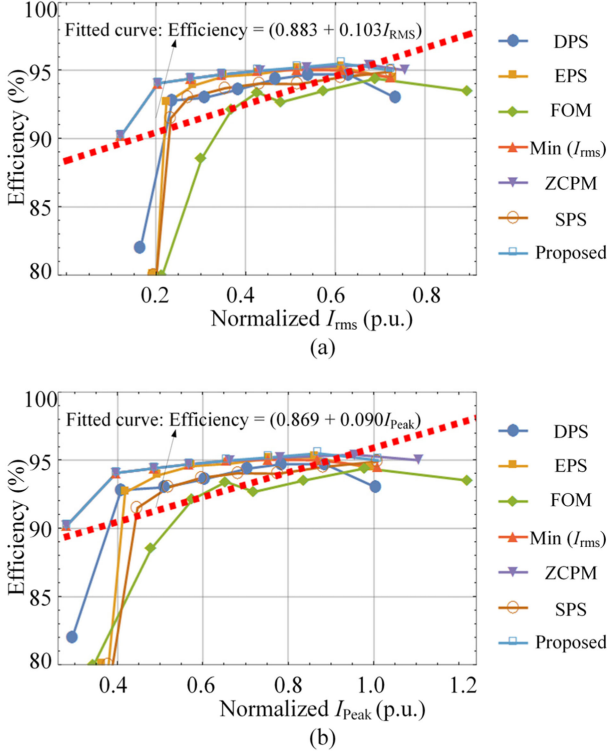


Fig. 24. (a) I_{rms} versus efficiency with multiple modulation schemes. (b) I_{Peak} versus efficiency with multiple modulation schemes.

In Fig. 23, the red dashed line is the fitted curve “Efficiency = $0.834 + 0.217A$ ” of multiple modulation schemes. When $A > 0.37$, the relation of A and efficiency shows good linearity. Apart from optimization objective A , all indicators in this article can be selected as the x -axis, and the comparison of the accuracy and linearity of indicators PF_{ab} , $\|p_{ab0c}\|_1$, $\|p_{ab0c}\|_2$, PF_{cd} , $\|p_{cd0c}\|_1$, $\|p_{cd0c}\|_2$, and optimization objective A versus efficiency curves are summarized in Table II.

In Table II, error-avg is the average error from the fitted curve and original data, standard error reflects the degree of dispersion of the original data set, T -statistic is for model coefficient significance test, and P -value is used to determine if the original hypothesis is correct.

The measured electric quantities I_{rms} and I_{Peak} are also selected as the x -axis, and the I_{rms} and I_{Peak} versus efficiency curves when $M = 0.8$ are depicted in Fig. 24.

Compared with Fig. 23, the I_{rms} and I_{Peak} versus efficiency curves are with less linearity. This is because both I_{rms} and I_{Peak} are usually higher with a higher P , but the efficiency

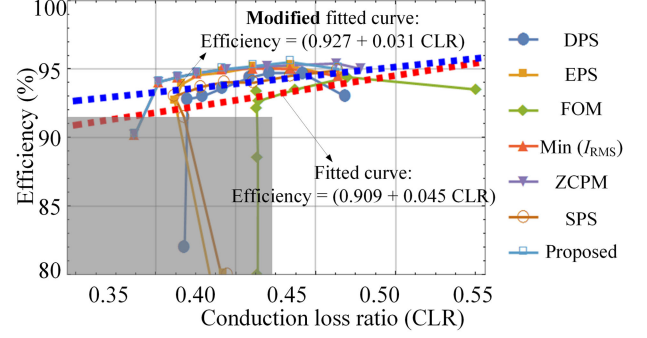


Fig. 25. CLR versus efficiency with multiple modulation schemes.

TABLE III
COMPARISON OF I_{rms} , I_{Peak} , AND CLR VERSUS EFFICIENCY CURVES

Indicators	Error-avg	Standard error	T-statistic	P-value
I_{rms}	0.023	0.026	3.996	2.0e-4
I_{Peak}	0.023	0.021	4.304	7.1e-5
CLR	0.024	0.033	1.371	1.8e-1
CLR (Modified)	0.009	0.009	3.285	1.9e-3

curve of DAB reaches its peak efficiency point at medium power condition and it goes down after this point. If we consider I_{rms} and P simultaneously, the conduction loss ratio (CLR) is defined in (32) to estimate the percentage of conduction loss for certain power transmission

$$CLR = \frac{I_{rms}^2}{P}. \quad (32)$$

The CLR versus efficiency curve when $M = 0.8$ is depicted in Fig. 25.

In Fig. 25, the CLR versus efficiency curve is very flat at high efficiency operation point (usually in medium and high power region), while it is extremely tilted for DPS, SPS, FOM, and EPS with low power region. When all experimental data are considered, the fitted curve is given as “Efficiency = $0.909 + 0.045 CLR$.” When the low efficiency operation points (DPS, SPS, FOM, and EPS when the output power is 0.8 kW) depicted in the shadow gray region are excluded, the modified fitted curve is given as “Efficiency = $0.927 + 0.031 CLR$.”

The accuracy and linearity of I_{rms} , I_{Peak} , CLR, and modified CLR versus efficiency curves are summarized in Table III.

Compare Tables II and III, the following conclusions can be drawn.

- 1) When optimization objective A (combination of indicators) is adopted to estimate the efficiency, smaller error-avg, standard error, P -value, and greater T -statistic are achieved. Hence, optimization objective A is better (higher accuracy, higher linearity, and lower dispersion) than a single indicator PF_{ab} , $\|p_{ab0c}\|_1$, $\|p_{ab0c}\|_2$, PF_{cd} , $\|p_{cd0c}\|_1$, or $\|p_{cd0c}\|_2$.
- 2) When single indicator is adopted to estimate the efficiency, $\|p_{ab0c}\|_1$ or $\|p_{ab0c}\|_2$ is better than PF_{ab} , and $\|p_{cd0c}\|_1$, or $\|p_{cd0c}\|_2$ is better than PF_{cd} .

- 3) Indicators PF_{ab} , $\|p_{ab0c}\|_1$, $\|p_{ab0c}\|_2$, PF_{cd} , $\|p_{cd0c}\|_1$, $\|p_{cd0c}\|_2$, and optimization objective A are better than I_{rms} , I_{Peak} , CLR, and modified CLR.
- 4) The estimation of efficiency with optimization objective A is with very high reliability and accuracy.

VI. CONCLUSION

HFL electric quantities are closely related to the performance of dc–dc converters. This article gives a general HFL analysis to guide the optimization of DAB. Instantaneous power is decomposed to dc power (average power) and fluctuation power. Novel indicators $\|p_{ab0c}\|_1$, $\|p_{ab0c}\|_2$, $\|p_{cd0c}\|_1$, and $\|p_{cd0c}\|_2$ with clear physical meaning are proposed from the perspective of signal strength and signal energy to measure dc power component percentage. A multiindicator evaluation system is established based on the proposed indicators and a hybrid optimization algorithm is proposed to calculate the optimal control coordinate. With the proposed optimal control coordinate, the efficiency of DAB is enhanced for most of the operation points. Besides, the proposed novel indicators and optimization objective A are also better at the estimation of efficiency compared with conventional I_{rms} and I_{Peak} .

DISCUSSION

The general HFL analysis can also be adopted in other converters like PSFB, series resonant converters, parallel resonant converters, LLC resonant converters, and LCC resonant converters, as long as the time domain waveforms can be described. The simplified HFL of PSFB is similar to that of DAB and the difference is that the indicator is much smaller. The general HFL analysis of resonant converters is a little different since resonant converters are with varying switching frequency. Denote the normalized switching frequency as F and replace ω with $F\omega$ in (1)–(10), indicators PF_{ab} , $\|p_{ab0c}\|_1$, $\|p_{ab0c}\|_2$, PF_{cd} , $\|p_{cd0c}\|_1$, and $\|p_{cd0c}\|_2$ can be obtained in a similar way.

APPENDIX

The expressions of \mathbf{S}_{abcc} , \mathbf{S}_{abcs} , \mathbf{S}_{absc} , and \mathbf{S}_{abss} are given as

$$\mathbf{S}_{abcc} = \mathbf{v}_{abc}^T \cdot \mathbf{i}_{zc} = \begin{bmatrix} a_{c1}c_{c1} & a_{c1}c_{c2} & \cdots & a_{c1}c_{cn} \\ a_{c2}c_{c1} & \ddots & \cdots & \vdots \\ \vdots & \cdots & \ddots & \vdots \\ a_{cn}c_{c1} & \cdots & \cdots & a_{cn}c_{cn} \end{bmatrix} \quad (\text{A1})$$

$$\mathbf{S}_{abcs} = \mathbf{v}_{abc}^T \cdot \mathbf{i}_{zs} = \begin{bmatrix} a_{c1}c_{s1} & a_{c1}c_{s2} & \cdots & a_{c1}c_{sn} \\ a_{c2}c_{s1} & \ddots & \cdots & \vdots \\ \vdots & \cdots & \ddots & \vdots \\ a_{cn}c_{s1} & \cdots & \cdots & a_{cn}c_{sn} \end{bmatrix} \quad (\text{A2})$$

$$\mathbf{S}_{absc} = \mathbf{v}_{abs}^T \cdot \mathbf{i}_{zc} = \begin{bmatrix} a_{s1}c_{c1} & a_{s1}c_{c2} & \cdots & a_{s1}c_{cn} \\ a_{s2}c_{c1} & \ddots & \cdots & \vdots \\ \vdots & \cdots & \ddots & \vdots \\ a_{sn}c_{c1} & \cdots & \cdots & a_{sn}c_{cn} \end{bmatrix} \quad (\text{A3})$$

$$\mathbf{S}_{abss} = \mathbf{v}_{abs}^T \cdot \mathbf{i}_{zs} = \begin{bmatrix} a_{s1}c_{s1} & a_{s1}c_{s2} & \cdots & a_{s1}c_{sn} \\ a_{s2}c_{s1} & \ddots & \cdots & \vdots \\ \vdots & \cdots & \ddots & \vdots \\ a_{sn}c_{s1} & \cdots & \cdots & a_{sn}c_{sn} \end{bmatrix} \quad (\text{A4})$$

REFERENCES

- [1] N. L. Kusters and W. J. M. Moore, "On the definition of reactive power under non-sinusoidal conditions," *IEEE Trans. Power App. Syst.*, vol. PAS-99, no. 5, pp. 1845–1854, Sep. 1980.
- [2] C. I. Budeanu, "Reactive and fictitious powers," (in Romanian) in *Instytut Romain de l'Energie*, No. 2, Bucharest, Rumania, 1927.
- [3] S. Fryze, "Active, reactive and apparent power in electrical circuits with non-sinusoidal course of current and voltage," (in German) *Elektrotechnische Zeitschrift*, vol. 53, no. 25, pp. 596–599, 1933.
- [4] S. M. Fryze, "Active, reactive and apparent powers in electric circuits with distorted voltages and currents, in Polish language," *Przełąd Elektrotechniczny*, vol. XIII, no. 7, pp. 193–203, 1931.
- [5] S. Fryze, "Active, non-active and apparent power in electrical circuits with nonsinusoidal time functions of current and voltage," (in German) *ETZ-A Elektrotech. Z.*, vol. 53, pp. 596–599, 1932.
- [6] H. Akagi, Y. Kanazawa, and A. Nabae, "Instantaneous reactive power compensators comprising switching devices without energy storage components," *IEEE Trans. Ind. Appl.*, vol. IA-20, no. 3, pp. 625–630, May 1984.
- [7] P. Tenti and P. Mattavelli, "A time-domain approach to power term definitions under non-sinusoidal conditions," *L'Energia Elettrica*, vol. 81, pp. 75–84, 2004.
- [8] P. Tenti, H. K. M. Paredes, and P. Mattavelli, "Conservative power theory, a framework to approach control and accountability issues in smart microgrids," *IEEE Trans. Power Electron.*, vol. 26, no. 3, pp. 664–673, Mar. 2011.
- [9] M. Aredes, H. Akagi, E. H. Watanabe, E. V. Salgado, and L. Frizera Encarnaç o, "Comparisons between the p–q and p–q–r theories in three-phase four-wire systems," *IEEE Trans. Power Electron.*, vol. 24, no. 4, pp. 924–933, Apr. 2009.
- [10] B. Zhao, Q. Yu, and W. Sun, "Extended-phase-shift control of isolated bidirectional DC–DC converter for power distribution in microgrid," *IEEE Trans. Power Electron.*, vol. 27, no. 11, pp. 4667–4680, Nov. 2012.
- [11] J. Deng, S. Li, S. Hu, C. C. Mi, and R. Ma, "Design methodology of LLC resonant converters for electric vehicle battery chargers," *IEEE Trans. Veh. Technol.*, vol. 63, no. 4, pp. 1581–1592, May 2014.
- [12] B. Gu, C. Lin, B. Chen, J. Dominic, and J. Lai, "Zero-voltage-switching PWM resonant full-bridge converter with minimized circulating losses and minimal voltage stresses of bridge rectifiers for electric vehicle battery chargers," *IEEE Trans. Power Electron.*, vol. 28, no. 10, pp. 4657–4667, Oct. 2013.
- [13] L. Xue, Z. Shen, D. Boroyevich, P. Mattavelli, and D. Diaz, "Dual active bridge-based battery charger for plug-in hybrid electric vehicle with charging current containing low frequency ripple," *IEEE Trans. Power Electron.*, vol. 30, no. 12, pp. 7299–7307, Dec. 2015.
- [14] H. Wang, S. Dusmez, and A. Khaligh, "Design and analysis of a full-bridge LLC-based PEV charger optimized for wide battery voltage range," *IEEE Trans. Veh. Technol.*, vol. 63, no. 4, pp. 1603–1613, May 2014.
- [15] F. Krismer and J. W. Kolar, "Accurate small-signal model for the digital control of an automotive bidirectional dual active bridge," *IEEE Trans. Power Electron.*, vol. 24, no. 12, pp. 2756–2768, Dec. 2009.
- [16] F. Krismer and J. W. Kolar, "Efficiency-optimized high-current dual active bridge converter for automotive applications," *IEEE Trans. Ind. Electron.*, vol. 59, no. 7, pp. 2745–2760, Jul. 2012.
- [17] T. Zhao, G. Wang, S. Bhattacharya, and A. Q. Huang, "Voltage and power balance control for a cascaded H-bridge converter-based solid-state

- transformer," *IEEE Trans. Power Electron.*, vol. 28, no. 4, pp. 1523–1532, Apr. 2013.
- [18] L. Wang, D. Zhang, Y. Wang, B. Wu, and H. S. Athab, "Power and voltage balance control of a novel three-phase solid-state transformer using multilevel cascaded H-bridge inverters for microgrid applications," *IEEE Trans. Power Electron.*, vol. 31, no. 4, pp. 3289–3301, Apr. 2016.
- [19] B. Zhao, Q. Song, J. Li, W. Liu, G. Liu, and Y. Zhao, "High-frequency-link DC transformer based on switched capacitor for medium-voltage DC power distribution application," *IEEE Trans. Power Electron.*, vol. 31, no. 7, pp. 4766–4777, Jul. 2016.
- [20] H. Shi *et al.*, "Minimum-backflow-power scheme of DAB-based solid-state transformer with extended-phase-shift control," *IEEE Trans. Ind. Appl.*, vol. 54, no. 4, pp. 3483–3496, Jul./Aug. 2018.
- [21] J. Liu, J. Yang, J. Zhang, Z. Nan, and Q. Zheng, "Voltage balance control based on dual active bridge DC/DC converters in a power electronic traction transformer," *IEEE Trans. Power Electron.*, vol. 33, no. 2, pp. 1696–1714, Feb. 2018.
- [22] B. Zhao, Q. Song, and W. Liu, "A practical solution of high-frequency-link bidirectional solid-state transformer based on advanced components in hybrid microgrid," *IEEE Trans. Ind. Electron.*, vol. 62, no. 7, pp. 4587–4597, Jul. 2015.
- [23] Z. Wang and H. Li, "A soft switching three-phase current-fed bidirectional DC-DC converter with high efficiency over a wide input voltage range," *IEEE Trans. Power Electron.*, vol. 27, no. 2, pp. 669–684, Feb. 2012.
- [24] Y. Shi, R. Li, Y. Xue, and H. Li, "Optimized operation of current-fed dual active bridge DC-DC converter for PV applications," *IEEE Trans. Ind. Electron.*, vol. 62, no. 11, pp. 6986–6995, Nov. 2015.
- [25] Q. Ye, R. Mo, and H. Li, "Low-frequency resonance suppression of a dual-active-bridge DC/DC converter enabled DC microgrid," *IEEE J. Emerg. Sel. Topics Power Electron.*, vol. 5, no. 3, pp. 982–994, Sep. 2017.
- [26] L. Wang, D. Zhang, Y. Wang, B. Wu, and H. S. Athab, "Power and voltage balance control of a novel three-phase solid-state transformer using multilevel cascaded H-bridge inverters for microgrid applications," *IEEE Trans. Power Electron.*, vol. 31, no. 4, pp. 3289–3301, Apr. 2016.
- [27] B. Zhao, Q. Song, W. Liu, G. Liu, and Y. Zhao, "Universal high-frequency-link characterization and practical fundamental-optimal strategy for dual-active-bridge DC-DC converter under PWM plus phase-shift control," *IEEE Trans. Power Electron.*, vol. 30, no. 12, pp. 6488–6494, Dec. 2015.
- [28] Q. Gu, L. Yuan, J. Nie, J. Sun, and Z. Zhao, "Current stress minimization of dual-active-bridge DC-DC converter within the whole operating range," *IEEE J. Emerg. Sel. Topics Power Electron.*, vol. 7, no. 1, pp. 129–142, Mar. 2019.
- [29] J. Huang, Y. Wang, Z. Li, and W. Lei, "Unified triple-phase-shift control to minimize current stress and achieve full soft-switching of isolated bidirectional DC-DC converter," *IEEE Trans. Ind. Electron.*, vol. 63, no. 7, pp. 4169–4179, Jul. 2016.
- [30] O. M. Hebala, A. A. Aboushady, K. H. Ahmed, and I. Abdelsalam, "Generic closed-loop controller for power regulation in dual active bridge DC-DC converter with current stress minimization," *IEEE Trans. Ind. Electron.*, vol. 66, no. 6, pp. 4468–4478, Jun. 2019.
- [31] N. Hou, W. Song, and M. Wu, "Minimum-current-stress scheme of dual active bridge DC-DC converter with unified phase-shift control," *IEEE Trans. Power Electron.*, vol. 31, no. 12, pp. 8552–8561, Dec. 2016.
- [32] N. Schibli, "Symmetrical multilevel converters with two quadrant dc-dc feeding," Ph.D. dissertation, Ecole Polytechnique Fédérale de Lausanne, Lausanne, Switzerland, 2000.
- [33] F. Krismer and J. W. Kolar, "Closed form solution for minimum conduction loss modulation of DAB converters," *IEEE Trans. Power Electron.*, vol. 27, no. 1, pp. 174–188, Jan. 2012.
- [34] A. Tong, L. Hang, G. Li, X. Jiang, and S. Gao, "Modeling and analysis of a dual-active-bridge-isolated bidirectional DC/DC converter to minimize RMS current with whole operating range," *IEEE Trans. Power Electron.*, vol. 33, no. 6, pp. 5302–5316, Jun. 2018.
- [35] Y. Xie, J. Sun, and J. S. Freudenberg, "Power flow characterization of a bidirectional galvanically isolated high-power DC/DC converter over a wide operating range," *IEEE Trans. Power Electron.*, vol. 25, no. 1, pp. 54–66, Jan. 2010.
- [36] D. Xu, C. Zhao, and H. Fan, "A PWM plus phase-shift control bidirectional DC-DC converter," *IEEE Trans. Power Electron.*, vol. 19, no. 3, pp. 666–675, May 2004.
- [37] H. Bai and C. Mi, "Eliminate reactive power and increase system efficiency of isolated bidirectional dual-active-bridge DC-DC converters using novel dual-phase-shift control," *IEEE Trans. Power Electron.*, vol. 23, no. 6, pp. 2905–2914, Nov. 2008.
- [38] B. Zhao, Q. Song, and W. Liu, "Power characterization of isolated bidirectional dual-active-bridge DC-DC converter with dual-phase-shift control," *IEEE Trans. Power Electron.*, vol. 27, no. 9, pp. 4172–4176, Sep. 2012.
- [39] B. Zhao, Q. Song, and W. Liu, "Efficiency characterization and optimization of isolated bidirectional DC-DC converter based on dual-phase-shift control for DC distribution application," *IEEE Trans. Power Electron.*, vol. 28, no. 4, pp. 1711–1727, Apr. 2013.
- [40] H. Wen, W. Xiao, and B. Su, "Nonactive power loss minimization in a bidirectional isolated DC-DC converter for distributed power systems," *IEEE Trans. Ind. Electron.*, vol. 61, no. 12, pp. 6822–6831, Dec. 2014.
- [41] H. Shi, H. Wen, Y. Hu, and L. Jiang, "Reactive power minimization in bidirectional DC-DC converters using a unified-phasor-based particle swarm optimization," *IEEE Trans. Power Electron.*, vol. 33, no. 12, pp. 10990–11006, Dec. 2018.
- [42] S. Shao, M. Jiang, W. Ye, Y. Li, J. Zhang, and K. Sheng, "Optimal phase-shift control to minimize reactive power for a dual active bridge DC-DC converter," *IEEE Trans. Power Electron.*, vol. 34, no. 10, pp. 10193–10205, Oct. 2019.
- [43] S. Wang, Z. Zheng, C. Li, K. Wang, and Y. Li, "Time domain analysis of reactive components and optimal modulation for isolated dual active bridge DC/DC converters," *IEEE Trans. Power Electron.*, vol. 34, no. 8, pp. 7143–7146, Aug. 2019.
- [44] H. Qin and J. W. Kimball, "Generalized average modeling of dual active bridge DC-DC converter," *IEEE Trans. Power Electron.*, vol. 27, no. 4, pp. 2078–2084, Apr. 2012.
- [45] J. A. Mueller and J. W. Kimball, "An improved generalized average model of DC-DC dual active bridge converters," *IEEE Trans. Power Electron.*, vol. 33, no. 11, pp. 9975–9988, Nov. 2018.
- [46] J. A. Mueller and J. W. Kimball, "Modeling dual active bridge converters in DC distribution systems," *IEEE Trans. Power Electron.*, vol. 34, no. 6, pp. 5867–5879, Jun. 2019.
- [47] S. R. Sanders, J. M. Noworolski, X. Z. Liu, and G. C. Verghese, "Generalized averaging method for power conversion circuits," *IEEE Trans. Power Electron.*, vol. 6, no. 2, pp. 251–259, Apr. 1991.
- [48] J. Everts, F. Krismer, J. V. D. Keybus, J. Driesen, and J. W. Kolar, "Optimal ZVS modulation of single-phase single-stage bidirectional DAB AC-DC converters," *IEEE Trans. Power Electron.*, vol. 29, no. 8, pp. 3954–3970, Aug. 2014.
- [49] G. Guidi, M. Pavlovsky, A. Kawamura, T. Imakubo, and Y. Sasaki, "Improvement of light load efficiency of dual active bridge DC-DC converter by using dual leakage transformer and variable frequency," in *Proc. IEEE Energy Convers. Congr. Expo.*, 2010, pp. 830–837.



Ziheng Xiao (Student Member, IEEE) was born in Zhejiang, China, in 1995. He received the B.S. degree from the College of Electrical and Information Engineering, Hunan University, Changsha, China in 2017. He is currently working toward Ph.D. degree in electrical engineering with the College of Electrical and Information Engineering, Hunan University, Changsha.

His research interests include dual active bridge converters, resonant converters, and dc/dc converter series and parallel operation and modular converter systems.



Zhixing He (Member, IEEE) was born in Hunan, China, in 1989. He received the B.S. degree in information science and engineering from Central South University, Changsha, China, in 2011, and the Ph.D. degree in electrical engineering from Hunan University, Changsha, China, in 2017.

From 2017 to 2018, he was with the Hunan University, as Postdoctoral Researcher. He is currently working as an Associate Professor with the College of Electrical and Information Engineering, Hunan University, Changsha. His research interests include

power electronics, medium voltage dc systems, model predictive control, and modular multilevel converters.



Hongliang Wang (Senior Member, IEEE) received the B.Sc. degree in electrical engineering from the Anhui University of Science and Technology, Huainan, China, in 2004, and the Ph.D. degree in electrical engineering from the Huazhong University of Science and Technology, Wuhan, China, in 2011.

From 2004 to 2005, he was an Electrical Engineer with Zhejiang Hengdian Thermal Power Plant, Zhejiang, China. From 2011 to 2013, he was a Senior System Engineer with Sungrow Power Supply Co., Ltd., Hefei, China. From 2013 to 2018, he was a

Postdoctoral Fellow with Queen's University, Kingston, ON, Canada. Since 2018, he has been with Hunan University, Changsha, China, where he is currently a Full Professor with the College of Electrical and Information Engineering. His research interests include multilevel topology, high-gain topology, parallel technology, and virtual synchronous generator technology for photovoltaic application and microgrids application, resonant converters and server power supplies, and LED drivers. He has authored more than 60 technical papers in journals and conferences. He is the inventor/co-inventor of 42 China issued patents and 8 US issued patents.

Dr. Wang is currently a Senior Member with China Electro-Technical Society, and also with China Power Supply Society (CPSS). He serves as a member of CPSS Technical Committee on Standardization, a member of CPSS Technical Committee on Renewable Energy Power Conversion, a China Expert Group Member of IEC Standard TC8/PT 62786, a Vice-Chair of IEEE Kingston Section, a Session Chair of ECCE 2015 and ECCE2017, and a TPC Member of ICEMS2012.



An Luo (Senior Member, IEEE) was born in Changsha, China, in 1957. He received the B.S. and M.S. degrees in industrial automation from Hunan University, Changsha, in 1982 and 1986, respectively, and the Ph.D. degree in fluid power transmission and control from Zhejiang University, Hangzhou, China, in 1993.

Between 1996 and 2002, he was a Professor with the Central South University, Changsha, China. Since 2003, he has been a Professor with the College of Electrical and Information Engineering, Hunan University, Changsha, China, where he also serves as the Chief of National Electric Power Conversion and Control Engineering Technology Research Center. His research interests include distributed generation, microgrids, and power quality.

Prof. Luo was elected to the Chinese National Academy of Engineering, the highest honor for scientists and engineers and scientists in China, in 2015. He was the recipient of the highly prestigious China National Science and Technology Award in 2014, 2010, and 2006.

Prof. Luo was elected to the Chinese National Academy of Engineering, the highest honor for scientists and engineers and scientists in China, in 2015. He was the recipient of the highly prestigious China National Science and Technology Award in 2014, 2010, and 2006.



Zhikang Shuai (Senior Member, IEEE) received the B.S. and Ph.D. degrees in electrical engineering from the College of Electrical and Information Engineering, Hunan University, Changsha, China, in 2005 and 2011, respectively.

He joined the Hunan University as an Assistant Professor in 2009, where he became an Associate Professor in 2013 and a Professor in 2014. His research interests include power quality control, power electronics, and microgrid stability analysis and control.

Dr. Shuai is the Associate Editor for the IEEE JOURNAL OF EMERGING AND SELECTED TOPICS IN POWER ELECTRONICS, and the *Chinese Journal of Electrical Engineering*. He is a recipient of the 2010 National Scientific and Technological Awards of China, the 2012 Hunan Technological Invention Awards of China, and the 2007 Scientific and Technological Awards from the National Mechanical Industry Association of China.



Josep M. Guerrero (Fellow, IEEE) received the B.S. degree in telecommunications engineering, the M.S. degree in electronics engineering, and the Ph.D. degree in power electronics from the Technical University of Catalonia, Barcelona, Spain, in 1997, 2000, and 2003, respectively.

Since 2011, he has been a Full Professor with the Department of Energy Technology, Aalborg University, Denmark. From 2015, he is a Distinguished Guest Professor with Hunan University, Changsha, China. His research interests include power electronics, distributed energy storage, and microgrids.

Prof. Guerrero is an Associate Editor for the IEEE TRANSACTIONS ON POWER ELECTRONICS, the IEEE TRANSACTIONS ON INDUSTRIAL ELECTRONICS, and the IEEE INDUSTRIAL ELECTRONICS MAGAZINE. He is also an Editor for the IEEE TRANSACTIONS ON SMART GRID and IEEE TRANSACTIONS ON ENERGY CONVERSION. He was the recipient of the Thomson Reuters as Highly Cited Researcher in 2014, 2015, and 2016, and was elevated as the IEEE Fellow for his contributions on distributed power systems and microgrids in 2015.

Prof. Guerrero is an Associate Editor for the IEEE TRANSACTIONS ON POWER ELECTRONICS, the IEEE TRANSACTIONS ON INDUSTRIAL ELECTRONICS, and the IEEE INDUSTRIAL ELECTRONICS MAGAZINE. He is also an Editor for the IEEE TRANSACTIONS ON SMART GRID and IEEE TRANSACTIONS ON ENERGY CONVERSION. He was the recipient of the Thomson Reuters as Highly Cited Researcher in 2014, 2015, and 2016, and was elevated as the IEEE Fellow for his contributions on distributed power systems and microgrids in 2015.